

# Gravitational Waves from Massive Black Hole Mergers in ASTRID: Predictions for LISA

BONNY Y. WANG (汪玥) <sup>1,2</sup> YIHAO ZHOU <sup>1</sup> WILLIAM CHEN <sup>1</sup> NIANYI CHEN <sup>3</sup> TIZIANA DI MATTEO <sup>1</sup>  
RUPERT CROFT,<sup>1</sup> SIMEON BIRD <sup>4</sup> AND YUEYING NI <sup>5</sup>

<sup>1</sup>*McWilliams Center for Cosmology and Astrophysics, Department of Physics, Carnegie Mellon University, Pittsburgh, PA 15213, USA*

<sup>2</sup>*Entertainment Technology Center, Carnegie Mellon University, Pittsburgh, PA 15213, USA*

<sup>3</sup>*School of Natural Sciences, Institute for Advanced Study, Princeton, NJ 08540, USA*

<sup>4</sup>*Department of Physics & Astronomy, University of California, Riverside, 900 University Ave., Riverside, CA 92521, USA*

<sup>5</sup>*Harvard-Smithsonian Center for Astrophysics, Harvard University, 60 Garden Street, Cambridge, MA 02138, USA*

## ABSTRACT

We use the ASTRID cosmological simulation to forecast massive black hole binary (MBHB) mergers detectable by LISA. ASTRID offers a detailed approach by directly modeling MBH dynamical friction, allowing for a more realistic tracking of their orbital evolution. Furthermore, it incorporates relatively low-mass MBH seeds down to  $5 \times 10^4 M_\odot$ , which provides a more complete picture of early MBH formation compared to other cosmological simulations. A key finding is the substantial increase in predicted LISA detection rates when MBH orbital eccentricity is considered, rising from 5.6/yr for circular orbits to 10.5/yr. This enhancement is largely due to the detectability of inspiral sources that will merge after LISA's observation period, which constitute 46% of detections in the eccentric scenario. This underscores the importance of LISA's sensitivity to the early inspiral phase, especially for eccentric binaries that emit gravitational waves across a wider frequency band. Most LISA events come from  $M_{\text{BH}} \sim 10^{5-6} M_\odot$ , low-redshift ( $z < 2$ ) and low mass-ratio ( $q \sim 0.01 - 0.1$ ) mergers, complementing observations from other instruments like Pulsar Timing Arrays (PTAs). Accounting for eccentricity also broadens the detectable MBH mass range to approximately  $10^9 M_\odot$  from  $10^8 M_\odot$ . It shifts the peak of detectable mergers to lower redshifts ( $z_{\text{peak}} = 0.8$  compared to 1.9 for circular orbits). Finally, this study indicates that LISA will detect MBH mergers in a diverse range of host galaxies, including lower-mass galaxies and satellite galaxies. The merger hosts are however fifty times more highly star-forming than the general population for the same mass, and we predict they should form a tight power-law sequence in  $\text{SFR}-M_{\text{gal}}$  space, with  $\text{SFR} = 10^{-8} M_{\text{gal}}^{0.9} M_\odot/\text{yr}$  independent of redshift. This contrasts with expectations for PTA sources, which are more likely to reside in massive central galaxies, implying that LISA will offer unique insights into MBH mergers occurring in different galactic environments. Only  $\sim 10\%$  of the remnant MBHs are bright AGNs, and most of them are from massive mergers with  $M_{\text{BH}} > 10^{6.5} M_\odot$ .

## 1. INTRODUCTION

Massive black holes (MBHs) are ubiquitous in the present Universe, harbored in almost all the massive galactic centers (Kormendy & Richstone 1995; Magorrian et al. 1998; Kormendy & Ho 2013). They play a major role in many aspects of galaxy evolution, and have a tight correlation with their host galaxies (Ferrarese & Merritt 2000; Graham et al. 2001; Ferrarese 2002; Gültekin et al. 2009; McConnell & Ma 2013; Reines &

Volonteri 2015; Greene et al. 2016; Schutte et al. 2019). Following the galaxies' merger, their central MBHs migrate toward the center of the remnant galaxy, losing the orbital energy and momentum via the dynamical friction and three-body scattering. After the MBH orbital decay to sub-parsec scales, the MBH binaries emit gravitational waves (GWs) and eventually coalesce (Merritt 2013). The GW signal emitted by the merging MBH offers a unique observational pathway for exploring the formation and evolution of MBHs (Wyithe & Loeb 2003; Sesana et al. 2007; Barausse 2012).

The Laser Interferometer Gravitational Wave Observatory (LIGO) detection reveals the population of stellar-mass black holes and validates using GWs to

study black hole binaries (Abbott et al. 2016). Recently, multiple Pulsar Timing Arrays (PTAs) have reported the first observation of GWs in the nanohertz frequency band (NANOGrav (Agazie et al. 2023); CPTA (Xu et al. 2023); PPTA (Reardon et al. 2023); EPTA+InPTA (EPTA Collaboration et al. 2023)), whose proposed sources are primarily expected to be MBH binaries with the mass of  $\gtrsim 10^8 M_\odot$  (Desvignes et al. 2016; Reardon et al. 2016; Arzoumanian et al. 2018). Different from LIGO and PTAs, the upcoming Laser Interferometer Space Antenna (LISA) mission will target the GWs signals among  $10^{-4} - 10^{-1}$  Hz, exploring the MBH mergers within the masses range  $10^4 - 10^7 M_\odot$  and up to redshifts of  $z \sim 20$  (Amaro-Seoane et al. 2017a).

To fully leverage the upcoming LISA detections, it is essential to develop sophisticated theoretical frameworks for merging MBH binaries and to make statistical predictions for the GW event rate. Major efforts have been made in this field in the last decade. Based on semi-analytical galaxy formation models and using black hole seed masses on the order of  $10^4 M_\odot$ , some works estimated that the merger rate ranges from 8 to over 20 per year (Arun et al. 2009; Sesana et al. 2011; Klein et al. 2016).

Some recent predictions are built from large-volume hydrodynamical simulations, which self-consistently follow the co-evolution of the MBH and their host galaxies across cosmic time, capturing nonlinear processes that cannot be described by simple analytical approximations. Such simulations can provide a more complete and consistent prediction of the MBH binary population. Combining the merging MBHs in the EAGLE simulation suite (Crain et al. 2015; Schaye et al. 2015) with the phenomenological frequency-domain gravitational waveform model PhenomD (Khan et al. 2016), Salcido et al. (2016) predicted  $\sim 2$  detections per year by LISA, and that the initial black hole seed mass could be distinguished through the detected gravitational waveforms. Katz et al. (2020) utilized the data from the Illustris cosmological simulation (Vogelsberger et al. 2014) and found a detection rate of  $\sim 0.5 - 1$  per year. High-resolution cosmological simulations, albeit with smaller volumes, have also been used as they can better resolve the dwarf galaxies hosting LISA sources (e.g. Tremmel et al. 2018; Volonteri et al. 2020; Li et al. 2022, 2023).

In this work, we study the MBH mergers that are detectable by LISA in the large-volume cosmological simulation ASTRID (Bird et al. 2022; Ni et al. 2022, 2024), which recently arrived at  $z = 0$ . ASTRID uses a novel power-law seeding with a range of MBH seed masses and so includes relatively low-mass MBH ( $\sim 5 \times 10^4 M_\odot$ ). More importantly, a subgrid model developed based on

Tremmel et al. (2015) and Chen et al. (2022a) is incorporated in ASTRID to track the MBH dynamical friction on the fly. This enables us to follow the MBH dynamics down to the resolution limit ( $\sim 1$  kpc), and to measure the realistic orbital evolution. These advantages put ASTRID in a unique position to be used to study MBH merging population. Chen et al. (2022b) and DeGraf et al. (2024) investigate the high-redshift ( $z > 2$ ) MBH mergers population and the host galaxies detectable by LISA. With ASTRID reaching down to  $z = 0$ , we now have the opportunity to examine sources at lower redshifts, to which LISA is most sensitive (Salcido et al. 2016; Izquierdo-Villalba et al. 2024).

This paper is organized as follows: in Section 2 we introduce the ASTRID simulation, and describe the methods used to calculate the GW signals. In Section 3 we present the MBH population in ASTRID, and make predictions for the LISA detection rate. In Section 4, we analyze the properties of the host galaxies and the MBH population of the LISA sources. We then discuss the implications and caveats of our results in Section 5 and conclude in Section 6.

## 2. METHODS

### 2.1. The ASTRID Simulation

ASTRID (Bird et al. 2022; Ni et al. 2022, 2024) is a large-volume cosmological hydrodynamical simulation performed using the Smoothed Particle Hydrodynamics (SPH) code MP-GADGET (Feng et al. 2018). The simulation evolves a cube of  $250 h^{-1} \text{cMpc}$  per side with  $2 \times 5500^3$  initial tracer particles comprising dark matter and baryons. The cosmological parameters used are from the Planck Collaboration et al. (2020) cosmology, with  $h = 0.6774$ ,  $\Omega_0 = 0.3089$ ,  $\Omega_\Lambda = 0.6911$ ,  $\Omega_b = 0.0486$ ,  $\sigma_8 = 0.816$ , and  $n_s = 0.9667$ . ASTRID has a mass resolution of  $M_{\text{DM}} = 6.7 \times 10^6 h^{-1} M_\odot$  and  $M_{\text{gas}} = 1.3 \times 10^6 h^{-1} M_\odot$  in the initial conditions. The gravitational softening length is  $e_g = 1.5 h^{-1} \text{ckpc}$  for both DM and gas particles. The initial conditions are set at  $z = 99$  and it has been evolved to  $z = 0$ .

ASTRID includes a full-physics sub-grid treatment for modeling galaxy formation, MBHs and their associated supernova AGN feedback, as well as inhomogeneous hydrogen and helium reionization. In the following we briefly list the sub-grid models relevant to MBH evolution. We refer readers to Bird et al. (2022) and Ni et al. (2022) for more details of the implemented models, and to Chen et al. (2022b) for a full description of the high-redshift merger catalog.

MBHs in ASTRID are seeded in halos with  $M_{\text{halo,FOF}} > 5 \times 10^9 h^{-1} M_\odot$  and  $M_{*,\text{FOF}} > 2 \times 10^6 h^{-1} M_\odot$ , with seed masses stochastically drawn from

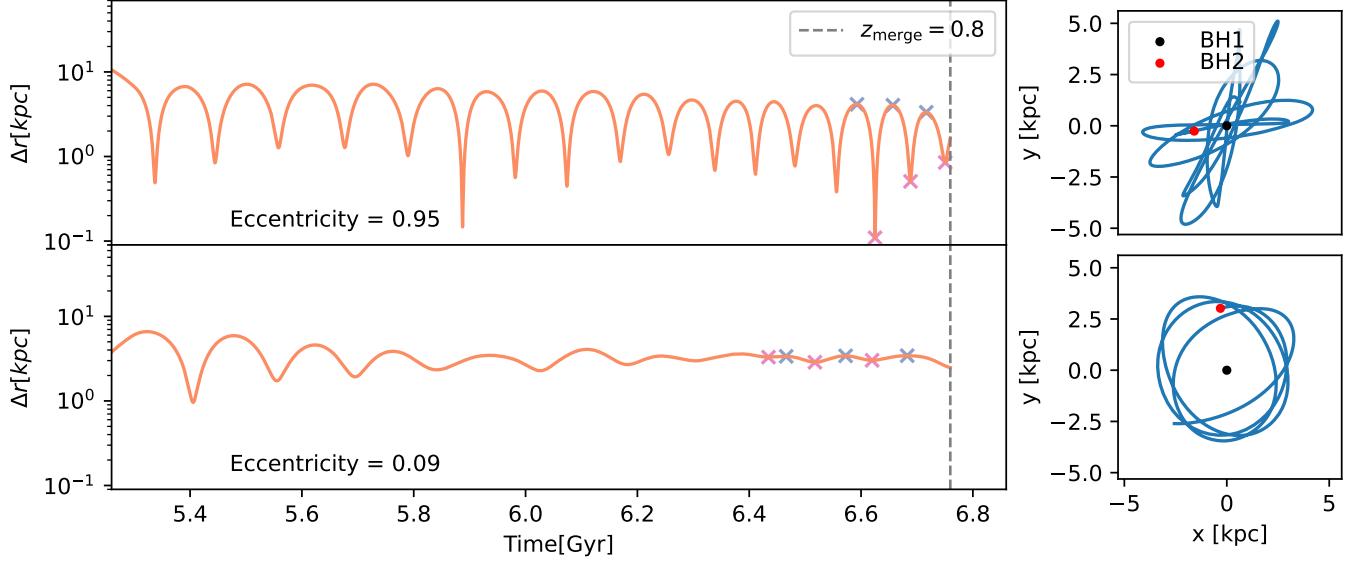


**Figure 1.** Examples of MBH mergers with a circular orbit ( $e = 0.09$ ; upper panel) and a highly eccentric orbit ( $e = 0.95$ ; lower panel) in ASTRID at  $z = 0.8$ . The plots on the left display the separation  $\Delta r$  between the two merging black holes as a function of time, with pink and blue crosses marking the last three pairs of  $r_{\text{apo}}$  and  $r_{\text{peri}}$  used to calculate the eccentricity values. The plots on the right show the corresponding orbital trajectories of the secondary black hole relative to the primary black hole’s position. The black and red dots mark the locations of the primary black hole (BH1) and the secondary black hole (BH2) before the merger.

the range  $3 \times 10^4 h^{-1} M_{\odot}$  to  $3 \times 10^5 h^{-1} M_{\odot}$ . The gas accretion rate  $\dot{M}_{\text{BH}}$  is estimated using the Bondi-Hoyle formalism (Bondi & Hoyle 1944). Super-Eddington accretion is allowed with an upper limit of twice the Eddington accretion rate. Each MBH radiates with a bolometric luminosity  $L_{\text{bol}}$  proportional to the accretion rate  $\dot{M}_{\text{BH}}$ , computed using a mass-to-energy conversion efficiency  $\eta = 0.1$  (Shakura & Sunyaev 1973). Of this, 5% of the radiated energy is thermally coupled to the gas within twice the radius of the SPH smoothing kernel of the black hole particle. A subgrid model is applied to estimate MBH dynamical friction following Tremmel et al. (2015) and Chen et al. (2022b). Compared to the more common implementation that directly repositions BHs to the local potential minimum (Weinberger et al. 2017), this model gives well-defined MBH trajectories and velocities. Two MBHs merge if their separation is within two times the gravitational softening length  $2e_g$ , once their kinetic energy is dissipated by dynamical friction and they are gravitationally bound to the local gravitational potential.

## 2.2. Shape measurement

In the ASTRID simulation, the trajectories of MBHs are output with high time resolution (every single simulation timestep). Having this fully sampled data leading up to each merger event enables accurate analysis of their orbital evolution. To measure the orbital eccen-

tricity  $e$ , we employ the shape measurement techniques described in Chen et al. (2022b), which we now briefly summarize. Taking the distance between the two merging black holes  $\Delta r$ , we define the periapsis  $r_{\text{peri}}$  to be its local minimum, and the apoapsis  $r_{\text{apo}}$  to be its local maximum. The eccentricity,  $e$ , is then given by:

$$e = \frac{r_{\text{apo}} - r_{\text{peri}}}{r_{\text{apo}} + r_{\text{peri}}}. \quad (1)$$

For each merger, we compute  $e$  from the three sets of  $r_{\text{apo}}$  and  $r_{\text{peri}}$  values that immediately precede the merger. We then select the maximum  $e$  from these three values to be the final measurement of  $e$  for each merger. This procedure minimizes the impact of falsely identified local extrema, which can produce unrealistically small  $e$ . Without this choice we would not correctly quantify the effect of incorporating eccentricity when compared to circular orbits. Figure 1 illustrates an example of a highly eccentric merging orbit ( $e \approx 1$ , upper panel) and a circularized orbit ( $e \approx 0$ , lower panel) at redshift 0.8. The left panels display  $\Delta r$  as a function of time, where the pink and blue crosses indicate the identified  $r_{\text{peri}}$  and  $r_{\text{apo}}$  values, which are used for the eccentricity calculation. The right panels show the corresponding orbits projected onto a plane perpendicular to the average relative velocity between the MBHs.

## 2.3. Gravitational Wave Signal Calculation

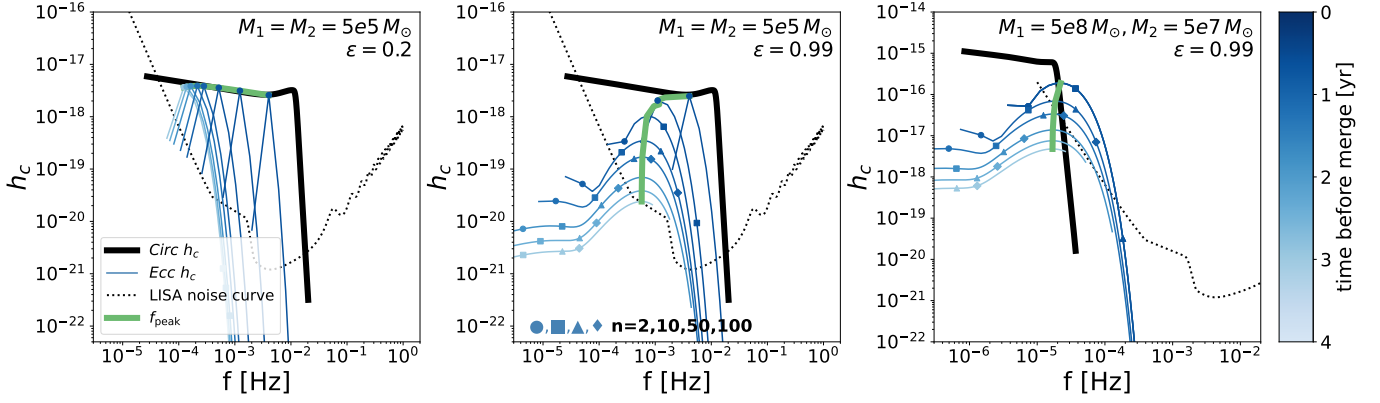


**Figure 2.** Waveforms for three binaries of different mass and orbital eccentricity  $e$  during the 4 years before the coalescence. The strain is calculated for  $z = 1$ , and the mass and the initial  $e$  are labeled on the upper right corner. In each panel, the black dotted line is the LISA instrument sensitivity curve with the galactic binary background. The thick black curve shows the strain assuming initial  $e = 0$ . The thin blue curves track the strain at different evolution times. The lines of constant time are shaded from light to dark for early to late evolution. On each blue curve, the circle, square, triangle, and diamond markers represent the evolution of individual harmonics:  $n=2, 10, 50$ , and  $100$ , respectively. The thick green curve plots the frequency having the highest strain  $f_{\text{peak}}$  for the eccentric waveforms during the evolution.

We use the `gwsnrcalc`<sup>1</sup> package (Katz & Larson 2019) to calculate the GW emitted by MBH mergers. We generate two sets of signals, one assuming circular orbits (labeled as *Circ*), and the other includes the orbital eccentricity measured in Section 2.2 (labeled as *Ecc*).

The *Circ* GW signals are from the PhenomD phenomenological model (Husa et al. 2016; Khan et al. 2016). This model requires input parameters such as the binary masses, the merger redshift, and the dimensionless spin of the binary components. The spin parameter  $a$  is a measure of the alignment between the spin angular momentum and the orbital angular momentum. Since  $a$  is not available in our simulation, we adopt a fixed spin value of  $a_1 = a_2 = 0.8$  for all binaries, as proposed in Katz et al. (2020) and used in many prior researches (e.g., Miller 2007; Reynolds 2013; Chen et al. 2022b; DeGraf et al. 2024). In PhenomD, the characteristic strain for a circular source,  $h_s$ , which accounts for the time the binary spends in each frequency ( $f$ ) bin, is defined as:

$$h_s(f) = 4f^2 |\tilde{h}(f)|^2, \quad (2)$$

where  $\tilde{h}(f)$  represents the Fourier transform of the time-domain signal (Finn & Thorne 2000; Moore et al. 2015).

For *Ecc*, gravitational wave strain is influenced by the orbital eccentricity. The  $h_s$  from an individual eccentric source can be related to that of a circular sources as (see Amaro-Seoane et al. 2010; Kelley et al. 2017; Chen et al.

2022b):

$$h_s^2(f_r) = \sum_{n=1}^{\infty} \left(\frac{2}{n}\right)^2 h_{r,\text{circ}}^2(f_h) g(n, e) \big|_{f_h=f_r/n}, \quad (3)$$

where  $h_{r,\text{circ}}$  is the characteristic strain for a circular source, as given in Equation 2.  $g(n, e)$  represents the GW frequency distribution function, defined by Equation 20 in Peters & Mathews (1963).

PhenomD describes the waveforms in the inspiral-merger-ringdown (IMR) phase in the  $l = m = 2$  quasinormal mode. For an eccentric binary merger, the inspiral waveforms are sufficiently accurate, but waveform models including the contributions from the merger and ringdown stages are less developed. Although recent efforts have been made to construct IMR waveforms with eccentricity (Hinder et al. 2018; Setyawati & Ohme 2021; Chattaraj et al. 2022), some important physical effects such as spin or higher order modes are not included, and there is still a lack of a clear and simple model to be implemented. Hence, to make a better comparison between the *Circ* and *Ecc* runs, in this work we only consider the waveforms from the inspiral phase while not including the emission during the phase of merger and ringdown.

To better assess the detectability of MBH binaries, we calculate the signal-to-noise ratio (SNR) for each merger. The SNR is determined by integrating the  $h_s$  above the LISA sensitivity curve over the frequency domain. Specifically, we compute the sky-averaged, orientation-averaged, and polarization-averaged SNR

<sup>1</sup> <https://pypi.org/project/gwsnrcalc/>



using the following expression:

$$\langle \text{SNR} \rangle^2 = \frac{16}{5} \int_{f_{\text{start}}}^{f_{\text{end}}} \frac{h_s^2}{h_N^2} f^{-1} df, \quad (4)$$

where  $f_{\text{start}} = f(t_{\text{start}})$  and  $f_{\text{end}} = f(t_{\text{end}})$ , with  $t_{\text{start}}$  and  $t_{\text{end}}$  denoting the beginning and end times of the observed signal.  $h_s$  is calculated based on Eq. 2 and Eq. 3 for **Circ** and **Ecc**, respectively.  $h_N$  is the strain of the LISA noise curve, which is from the LISA Mission Proposal (Amaro-Seoane et al. 2017b). In this work, we include the effect of galactic background noise in addition to the LISA instrumental noise, for which we use the analytical approximation from Hiscock et al. (2000). For each merger, we assume an observation period of 4 years and calculate the most optimistic SNR by setting  $t_{\text{end}} = t_{\text{peak}}$  and  $t_{\text{start}} = t_{\text{peak}} - 4$  yr. In this work, we classify mergers with  $\text{SNR} > 10$  as sources detectable by LISA.

In Figure 2, we show the waveforms for three binaries with different masses and orbital eccentricities  $e$  during the four years before coalescence. The strain is calculated for  $z = 1$ , and the mass and the initial  $e$  are labeled in the upper right corner. In each panel, the black dotted line is the LISA instrument sensitivity curve with the galactic binary background. The thick black curve shows the strain assuming initial  $e = 0$ . The thin blue curves track the strain at different evolution times. The lines of constant time are shaded from light to dark for early to late evolution. On each blue curve, the circle, square, triangle, and diamond markers represent the evolution of individual harmonics:  $n=2, 10, 50$ , and  $100$ , respectively. The thick green curve plots the frequency having the highest strain  $f_{\text{peak}}$  for the eccentric waveforms during the evolution. For the binaries with the circular orbit, the strain comes from the individual harmonic mode  $n = 2$ ; while for the eccentric binaries, the GW signal is contributed by all  $n \geq 1$  harmonic modes, which produces a wide frequency range. As we will discuss later in Section 2.4, this boosts the detectability for some massive or low- $z$  sources. The eccentricity decays with the GW emission (Peters & Mathews 1963), which is called circularization. This makes the waveforms shortly before the coalescence similar to those from circular binaries (black thick curves), and the dominant frequency  $f_{\text{peak}}$  evolves towards the  $n = 2$  mode (blue circles).

As can be seen from Fig. 2, the signal from high harmonic modes ( $n \geq 2$ ) is important for the high-eccentricity sources. For binaries with  $e = 0.99$ , the dominant mode at 4 years before the coalescence is larger than  $n=100$  (see the low-frequency end of the  $f_{\text{peak}}$  curves). To ensure we have sufficient harmonic

modes for the high-eccentricity sources while keeping the computational cost reasonable, we truncate the summation in Eq. 3 at  $n_{\text{max}}$  for the sources in **Ecc** run, and vary the value of  $n_{\text{max}}$  with the initial eccentricity  $e_0$ . To determine  $n_{\text{max}}$ , we first search for the dominant harmonic mode  $n_{\text{dom}}(e_0)$ , which has maximum  $g(n, e_0)/n$  and is independent of the mass or redshift for specific sources (Wagg et al. 2022). We then set  $n_{\text{max}} = 2 \times n_{\text{dom}}$  with a minimum value of  $n = 50$ , i.e.,  $n_{\text{max}} = \max(2 \times n_{\text{dom}}, 50)$ .

#### 2.4. Merger rate prediction

To estimate the LISA detection rate, we follow Katz et al. (2020) and implement the Monte Carlo analysis technique. This enables us to generate multiple realizations of the merger population detected by LISA. In the following we briefly summarize this method and refer readers to Katz et al. (2020) for more details.

Based on the MBH population in ASTRID, the MBH merger rate is defined as the number of merging MBH systems observed per year per unit redshift, which can be estimated from:

$$\frac{d^2 N(z)}{dz dt} = \frac{\Delta N}{\Delta z} \frac{dV_c(z)}{V_{\text{sim}} dt} \frac{1}{1+z}, \quad (5)$$

where  $dV_c(z)$  is the comoving volume element of the Universe at a given redshift, and  $V_{\text{sim}}$  is the comoving volume of ASTRID simulations.  $\Delta N(z)$  is the number of mergers in a specific redshift bin, whose width is  $\Delta z$ . For each MBH merger in ASTRID, its contribution to the merger population observed within a  $t_{\text{dur}}$  time window is

$$\lambda_i = t_{\text{dur}} \frac{dV_c(z_i)}{V_{\text{sim}}} \frac{1}{1+z_i}, \quad (6)$$

where  $z_i$  is the merger redshift of the MBH binary  $i$ . The expected total source number for one realization of the observed MBH merger population is then given by

$$\langle N_{t_{\text{dur}}} \rangle = \frac{t_{\text{dur}}}{V_{\text{sim}}} \sum_i \lambda_i \frac{dV_c(z_i)}{1+z_i}, \quad (7)$$

where  $\sum_i$  denotes the sum over all the mergers in ASTRID. To generate multiple realizations, we draw values from the Poisson distribution centered at  $\lambda_i$ :  $\mathcal{P}(\lambda_i)$  to determine whether the binary  $i$  is included in specific realizations or not. Hence, the number of sources for one realization is

$$N_{t_{\text{dur}}} = \frac{t_{\text{dur}}}{V_{\text{sim}}} \sum_i \mathcal{P}(\lambda_i) \frac{dV_c(z_i)}{1+z_i}. \quad (8)$$

Specifically, if  $\mathcal{P}(\lambda_i) \geq 2$ , we use the same binary parameters (e.g., the MBH masses, merger redshift, and

eccentricity) for the duplicated mergers to calculate the expected GW emission. In this work, we generate 10,000 realizations to predict the LISA detection rate.

An advantage of implementing this Monte Carlo analysis is that we can include the GW signals emitted by the inspiral sources, which coalesce after the LISA mission ends. To do this, we sample the MBH populations merging within  $t_{\text{dur}}$ , and the first  $t_{\text{obs}}$  phase ( $t_{\text{dur}} > t_{\text{obs}}$ ) corresponds to the observation time. The binaries which take less time than  $t_{\text{obs}}$  to merge are marked as ‘merger sources’ (these are observed to coalesce). The binaries which merge after  $t_{\text{obs}}$  are labeled as ‘inspiral sources’ as they keep inspiraling during the whole observation phase. For the LISA mission,  $t_{\text{obs}} = 4$  years. Following Katz et al. (2020), we set  $t_{\text{dur}} = 100$  years<sup>2</sup>. As the Universe evolves negligibly over  $t_{\text{dur}}$ , we can assume that the merger times of the  $N_{t_{\text{dur}}}$  sources are uniformly distributed over the interval of length  $t_{\text{dur}}$ . We therefore draw the observation start  $t_{\text{start}}$  randomly from between 0 and 100 years to decide which 4-year phase for an individual merger is observed during  $t_{\text{dur}}$  beyond coalescence. For the observation end time  $t_{\text{end}}$ ,  $t_{\text{end}} = t_{\text{start}} - t_{\text{obs}}$  if  $t_{\text{start}} > t_{\text{obs}}$  (inspiral sources); and  $t_{\text{end}} = 0$  if  $t_{\text{start}} \leq t_{\text{obs}}$  (merger sources). GW signals from  $t_{\text{start}}$  to  $t_{\text{end}}$  before the coalescence are used to calculate the SNR for each merger.

### 3. RESULTS

In this section, we present the merging MBH populations in the ASTRID simulation, and make predictions for the sources to be detected by the LISA mission.

#### 3.1. MBH population in ASTRID

In Figure 3, we present an illustration of LISA sources in a slice of  $100 \times 60 \times 10 \text{ Mpc}^3 h^{-3}$  extracted from ASTRID at  $z = 0.8$ . The upper panel illustrates the gas density field color-coded by the temperature, with warmer regions corresponding to higher temperatures. Yellow circles mark the locations of the mergers occurring within a 670 Myr period centered on  $z = 0.8$ . We select five merging systems as examples, which cover the whole mass range ( $10^5 \sim 10^8 M_{\odot}$ ) for the LISA sources, and mark their position with arrows. The middle panels show the stellar density field of the host halo for the five systems, color-coded by stellar age, where blue regions represent young stars. The red crosses show the position of the primary MBH (or the remnant MBH), and the green crosses show the secondary MBH. The bottom

panels show their host galaxy, with the RGB channels representing the flux in the rest-frame *grz* color bands.

In the upper panel of Figure 4, we present the black hole mass function (BHMF) in ASTRID at different redshifts ( $z = 0.0, 1.0, 2.0, 4.0, 6.0$ ). The BHMF is defined as the number density of black holes per unit comoving volume as a function of their mass, expressed as  $\Phi(M_{\text{BH}}, z) = \frac{dN}{d(\log M_{\text{BH}})dV_c}$ , where  $dN$  is the number of black holes within a mass bin,  $d(\log M_{\text{BH}})$  is the width of that mass bin, and  $dV_c$  is the comoving volume element at  $z$ . It can be seen that at lower redshifts, there is an increasing abundance of MBHs. The peak of the distribution shifts from the seed mass range ( $10^5 M_{\odot}$ ) at  $z = 6.0$  to approximately  $10^6 M_{\odot}$  at  $z < 1.0$ . The lower panel shows the ratio of the number of merged black holes to the total black hole population. At the lower mass end, the MBHs merge less efficiently at lower redshifts after  $z = 2$ . This can be explained by the lower galaxy merger rate at low-redshift (Rodríguez-Gomez et al. 2015).

In Figure 5 we present the merging orbit eccentricity  $e$  distributions, which are estimated based on the method described in Section 2.2. The left panel shows the probability density function (PDF) for  $e$  at different redshifts. Across the whole redshift range,  $e$  peaks at high values:  $e \gtrsim 0.8$ , and it evolves to a smaller value at lower redshift: from 0.88 at  $z > 3$  to 0.80 at  $z < 0.5$ , indicating a larger fraction of binaries at low redshift merge with circular orbits. A potential explanation for this evolution is that binaries with eccentric orbits have shorter hardening timescales (Chen et al. 2022b) and they will merge shortly after the binaries are formed, while many circular binaries keep evolving towards lower redshift. To give a better description of the  $e$  distribution, we fit the PDF shown in Fig. 5 using a  $\beta$  distribution:

$$f(e) = \mathcal{N} e^{\alpha-1} (1-e)^{\beta-1}, \quad 0 \leq e \leq 1. \quad (9)$$

The normalization factor is  $\mathcal{N} = 1/B(\alpha, \beta)$ , where  $B(\alpha, \beta)$  is the  $\beta$  function. The two shape parameters  $\alpha$  and  $\beta$  depend linearly on redshift  $z$ :  $\alpha = 1.08(1+z) + 2.08$ ,  $\beta = 0.07(1+z) + 1.56$ . The fitted distributions are plotted in Figure 5 with dotted curves. The right panel shows the PDF within different total MBH masses. Although the evolution of  $e$  over  $M_{\text{BH}}$  is less obvious compared to that over  $z$ , we note that the most massive mergers  $M_{\text{tot}} > 10^8 M_{\odot}$  typically have higher  $e$ .

#### 3.2. LISA Predictions

In this subsection, we investigate the MBH mergers in the Circ/Ecc run that are detectable by LISA (i.e.,

<sup>2</sup> We test different choices of  $t_{\text{dur}}$ , and confirm that our prediction results converge with  $t_{\text{dur}} \geq 100$  yr.

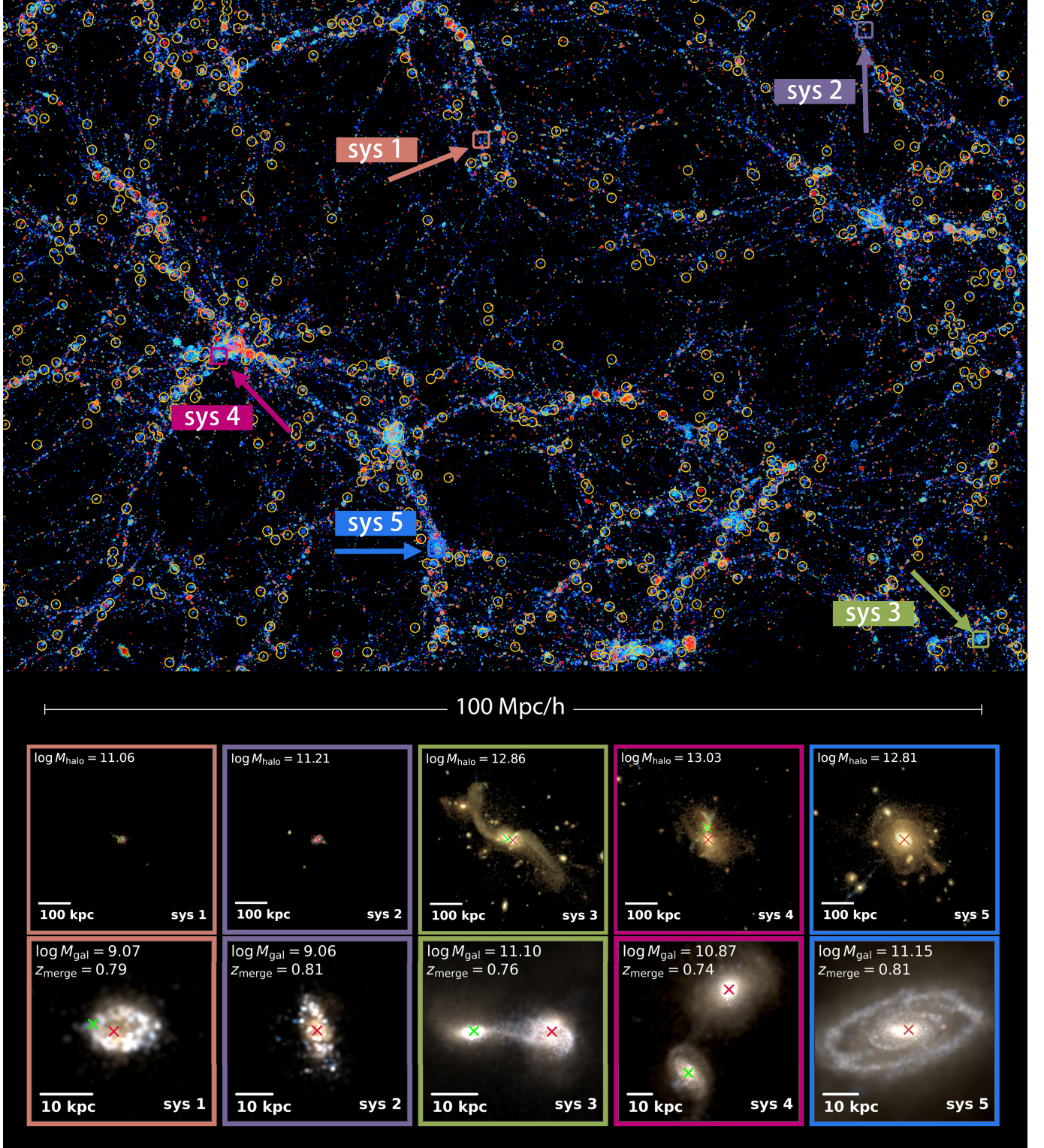


**Figure 3.** Illustration of ASTRID at  $z = 0.8$ . The upper panel shows the large-scale structure in a slice of  $100 \times 60 \times 10 \text{ Mpc}^3 h^{-3}$ , with gas temperature represented by color: hotter regions appear in red, while cooler regions are shown in blue. Yellow circles mark the locations of detectable mergers (i.e., with  $\text{SNR} > 10$ ) occurring within the 670 Myr around  $z = 0.8$ . Five merging systems are selected as examples, whose positions are marked in the plot. The middle panels show the stellar density field within 600 Mpc/h around the merging MBH binaries, color-coded by the stellar age, where blue regions represent young stars. The red crosses show the position of primary MBH (or the remnant MBH), the green crosses show the secondary MBH. The bottom panels show the host galaxy of the merging MBHs, with the RGB channels representing the flux in the rest-frame  $grz$  color bands.



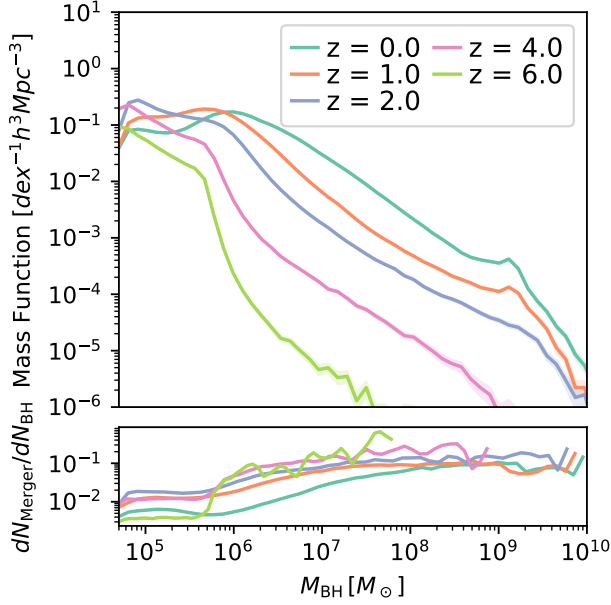


**Figure 4.** The MBH population in ASTRID at different redshifts. *Upper* : The black hole mass function in terms of comoving number density ( $\text{dex}^{-1} h^3 \text{Mpc}^{-3}$ ). *Lower* : The ratio between the number of the MBH involved in mergers and the total MBH.

with  $\text{SNR} > 10$ ), and make predictions for the LISA detection rate.

We take the waveforms calculated in Section 2.3, and compute the strain and frequency distributions for the MBH mergers in ASTRID. The results are shown in Fig. 6, where the left panel is for the *Circ* run and the right panel for the *Ecc* run. For each MBH merger, we find the point in its time evolution and the harmonic mode that makes the greatest contribution to the SNR in the 4 years before coalescence. This is used to position the source in Fig. 6. For the *Circ* run, the harmonic mode is always  $n = 2$ . We color the distribution based on the redshift and the number of events, as shown by the right colorbar: the high (low) redshifts are represented by blue (red) colors, and the darkness corresponds to the regions with very few events. The redshift is averaged over the merger population within each pixel. The cut around  $f \sim 10^{-2.5}$  Hz corresponds to the LISA sensitivity peak, which arises from our choice of plotting the frequency that contributes the most to the SNR. As we can see, the strain-frequency distributions for the *Circ* and *Ecc* runs are generally similar, except that the scatter in the strain range for a specific redshift is slightly larger for *Ecc* run.

In Fig. 7, we demonstrate the parameter space of MBH mass and redshift explored by LISA. The left panel shows the two-dimensional distribution of red-

shift and total merger mass  $M_{\text{tot}}$ , and the right panel shows how the mass of the primary MBH  $M_1$  and secondary MBH  $M_2$  are distributed. The underlying blue color gradient represents the differential number of the detected mergers during the LISA 4-year observation for *Ecc* run:  $dN/(d \log M dz dt) \times 4\text{yr}$  for the left panel and  $dN/(d \log M_1 d \log M_2 dt) \times 4\text{yr}$  for the right panel. The black and red contours correspond to the detected MBH merger population for *Ecc* run and *Circ* run, respectively. We can see that the detected eccentric and circular binaries largely overlap, and most of the LISA sources are low-mass mergers with  $M_{\text{tot}} < 10^7 M_\odot$  at the local Universe ( $z < 2$ ). An important difference between *Ecc* and *Circ* observed in Fig. 7 is that including eccentricity enables LISA to explore sources with higher mass. Around  $z \sim 0$ , the most massive mergers within detectable circular binaries have mass  $\sim 10^8 M_\odot$ , while for eccentricity sources, the high-mass limit increases to  $M_{\text{tot}} \sim 10^9 M_\odot$ . This is also supported by the  $M_2 - M_1$  distribution plot: in *Ecc* run, the covered mass spectra is increased by one order of magnitude compared to the *Circ* run.

We next make predictions for the LISA detection rate based on the prescription described in Section 2.4. We generate 10,000 realizations of the merging MBH population, and present the averaged detection rate in Fig. 8. In the left (right) column, we show the number of observed sources, i.e., with the  $\text{SNR} > 10$ , per year per unit redshift (per unit  $\log M_{\text{BH}}$ ). In the upper panels, the solid blue and yellow curves represent the results for the *Ecc* and *Circ* runs, respectively. Specifically, we use the blue dashed curve to denote the contribution from the inspiral sources in the *Ecc* run. We do not plot the inspiral sources for *Circ* since only a negligible number are detectable (less than  $10^{-3}/\text{yr}$ ), which is consistent with Katz et al. (2020) (see their Table A1). In the lower panels, we show the ratio between the number of detectable sources in *Circ* and *Ecc*. We mark  $N_{\text{Ecc}} = N_{\text{Circ}}$  with a black dashed line. If we consider the detection rate per unit redshift,  $d^2 N/dz dt$ , we observe that the *Circ* and *Ecc* runs peak at different redshifts:  $z_{\text{peak}} = 1.9$  for *Circ* and  $z_{\text{peak}} = 0.80$  for the *Ecc* run (marked by the vertical yellow and blue dotted lines, respectively). At low redshift ( $z < 2$ ), incorporating eccentricity significantly increases the detection rate, and  $z \sim 0$ , the ratio  $N_{\text{Ecc}}/N_{\text{Circ}}$  is larger than 10. As for the detection rate across the  $M_{\text{BH}}$  (right column), both *Ecc* and *Circ* runs peak at the lower mass end, as expected. The plateau at  $M < 10^6 M_\odot$  and the cut at  $10^5 M_\odot$  come from the black hole seed mass adopted in ASTRID. In *Ecc* run, the number of detected sources at high mass end ( $M_{\text{BH}} > 10^{7.5} M_\odot$ ) is increased by more than one order



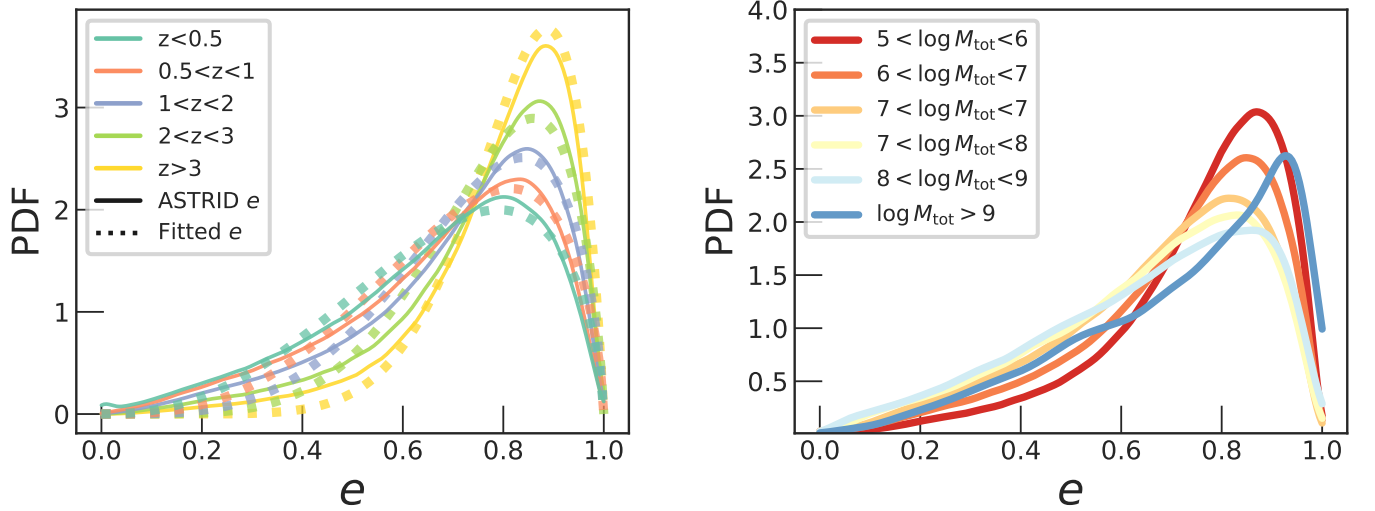


**Figure 5.** Probability density function (PDF) of merger orbit eccentricities  $e$  measured based on Eq. 1. *Left:* PDF for mergers at different redshifts. Solid curves represent the distribution from ASTRID merger population, and dotted curves show the fitted  $\beta$  distribution (Equ. 9) for the redshifts with the corresponding color. *Right:* PDF for mergers with different total MBH masses.

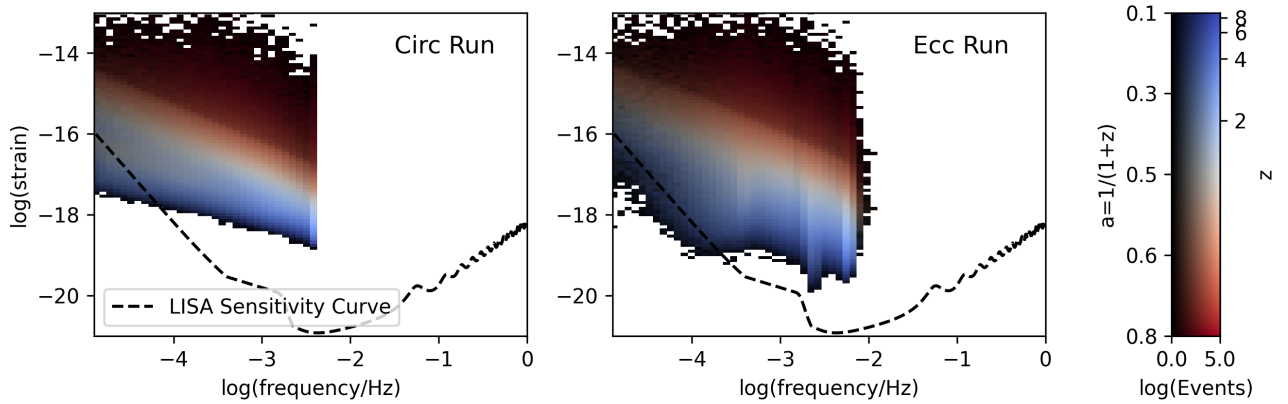


**Figure 6.** Strain and frequency distribution for the mergers in ASTRID. The left frame is for **Circ** run and the right panel is for **Ecc** run. For each MBH merger, the plotted frequency and strain correspond to the evolution time point and harmonic mode that makes the largest contribution to SNR within 4 years before the coalescence. For the **Circ** run, the harmonic mode is always  $n = 2$ . We color the distribution based on the redshift and the number of events, as shown by the right colorbar: the high(low) redshifts are represented by the blue(red) colors, and the darkness corresponds to the regions with very few events. The redshift is averaged over the merger population in each pixel.

of magnitude, and the part of the mass spectrum that can be explored expands from  $10^8 M_\odot$  in the **Circ** run to  $10^9 M_\odot$  in the **Ecc** run. Summed over redshift, the total LISA detection rate predicted by ASTRID is 5.6/yr for the **Circ** run and 10.5/yr for the **Ecc** run. Among the events, 46% (4.8 per year) are inspiral sources for **Ecc**, and only 0.3% ( $\sim 10^{-3}$  per year) for **Circ**.

An important message we can get from Fig. 8 is that incorporating orbital eccentricity boosts the LISA detectability. Such an enhancement comes almost fully from the inspiral sources: the number of detected merger sources is almost the same in the **Ecc** run (5.7/yr) and

in the **Circ** run (5.6/yr). In the **Ecc** run, at low redshift ( $z < 0.5$ ) or at the high mass end  $M > 10^{7.5}$ , the detected inspiral sources outnumber the merger sources by almost an order of magnitude. For the inspiral sources, as the frequency evolution during the early stages is typically slow (Sesana 2010), the covered frequency range for an individual harmonic mode is very narrow, producing a smaller SNR for the inspiral sources in the **Circ** run. On the other hand, in the **Ecc** run, the harmonic modes higher than  $n > 2$  not only result in a wider frequency range but also extend the signal to the band where LISA has high sensitivity (see the right panel of

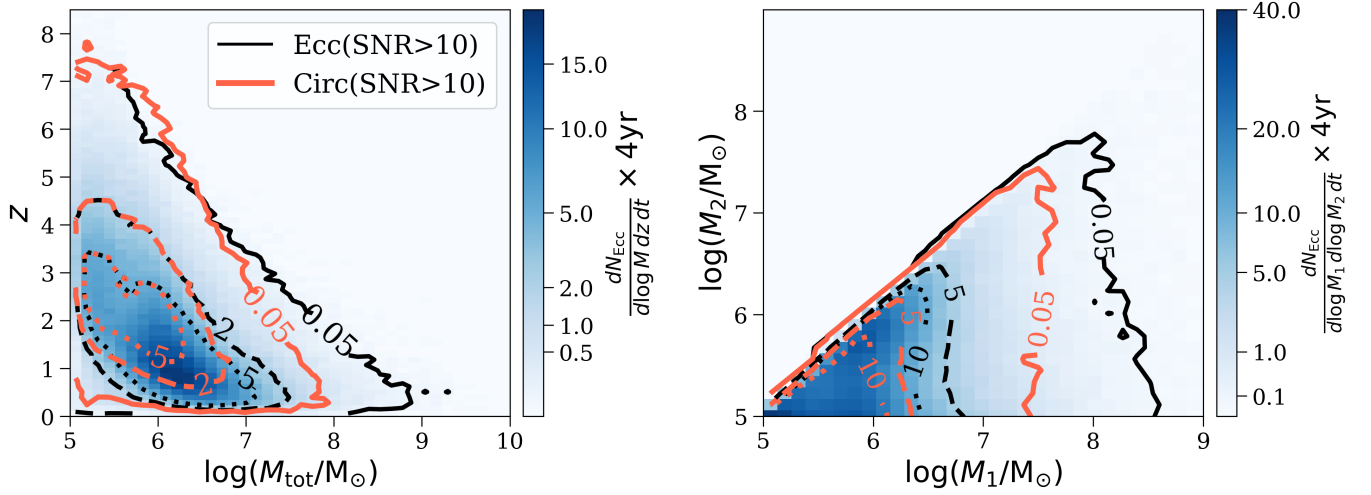


**Figure 7.** Parameter space of MBH mass and redshift explored by LISA. The left panel plots the two-dimensional distribution of the redshift and the total mass of merging MBHs  $M_{\text{tot}}$ . The right panel shows the distribution of the mass of the primary MBH  $M_1$  and the secondary MBH  $M_2$ . The underlying blue color gradient represents the differential number of detected mergers during the LISA 4-year observation for Ecc run:  $dN/(d \log M dz dt) \times 4\text{yr}$  for the left panel and  $dN/(d \log M_1 d \log M_2 dt) \times 4\text{yr}$  for the right panel. The black and red contours correspond to the detected MBH merger population for Ecc run and Circ run, respectively.

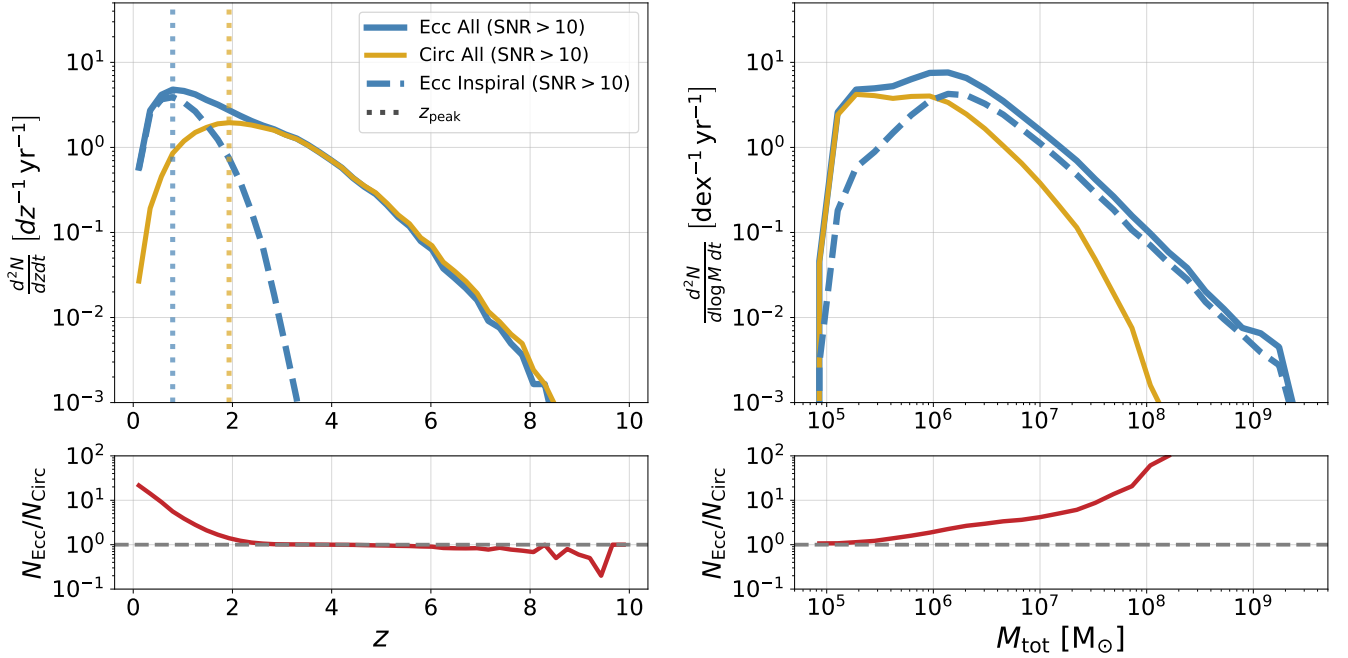


**Figure 8.** The LISA detection rate estimated using 10,000 realizations of MBH population. *Upper* : the number of observed binaries (with  $\text{SNR} > 10$ ) per year per unit redshift (left) /  $\log M_{\text{BH}}$  (right). In each panel, the yellow/blue solid curves represent the results from Circ/Ecc run, respectively. The blue dashed curve shows the predicted inspiral sources from the Ecc runs. We do not plot the inspiral sources for the Circ since it has a negligible number of inspiral sources (less than  $10^{-3}/\text{yr}$ ). In the upper left frame, the vertical dotted line represents the peak of redshift distribution:  $z_{\text{peak}} = 1.9$  for Circ (yellow) and  $z_{\text{peak}} = 0.80$  (blue) for Ecc run. *Bottom* : the fraction between the number of detectable sources in Circ and Ecc. We mark the level of  $N_{\text{Ecc}} = N_{\text{Circ}}$  with the black dashed line.

Fig. 2). This makes the inspiral sources more likely to be detected when the eccentricity is taken into account.

A caveat is that at  $z > 2$  or  $M_{\text{BH}} < 10^6 M_\odot$ , the number of detectable inspiral sources drops quickly. This is

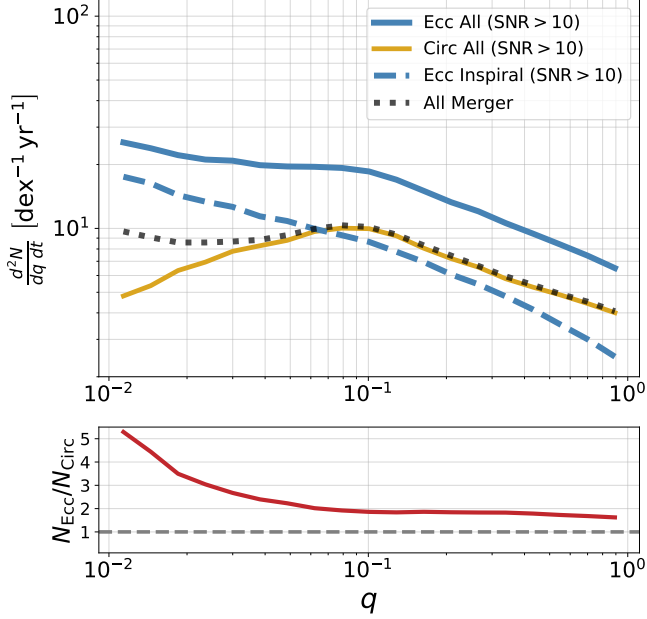


**Figure 9.** Same with Fig. 8 but the detection rate is plotted as a function of the mass ratio  $q = M_2/M_1$ . The black dotted curve in the upper panel represents all the merger sources in ASTRID.

because at high redshift, or the low mass end, the strain is too low to produce a detectable signal even if the high harmonic mode is close to the LISA high-sensitivity band. Moreover, for the eccentricity binaries, their peak strain is lower than their circular counterpart, which can be seen from Fig. 2 (middle and right panels). This explains why at high redshift ( $z > 6$ ), **Circ** run predicts a slightly larger detection rate than the **Ecc** run. The mass peak for the inspiral sources at  $M_{\text{tot}} \sim 10^6 M_\odot$  shifts the entire distribution of detectable sources in the **Ecc** run to slightly higher mass. In the **Circ** run, where almost all the sources are merger sources, the mass peak is around the black hole seed mass  $M_{\text{tot}} \sim 10^5 M_\odot$ .

The minor increase in the number of detected merger sources in the **Ecc** run (from 5.6/yr in **Circ** run to 5.7/yr) is from massive mergers. With the circular orbit assumption, no mergers with  $M_{\text{tot}} > 10^8 M_\odot$  can be detected, while in the **Ecc** run, there are still some sources with  $M_{\text{BH}} \gtrsim 10^9 M_\odot$  observed through coalescence in the 4-year observation. This corresponds to the gap between the blue solid curve and the blue dashed curve. Binaries with such a large mass typically merge at low frequency before they are observed in the LISA band. When we include the eccentricity, the higher harmonic modes increase the emission at higher frequency, which is closer to the LISA high-sensitivity band, and this contributes significantly to the total SNR. This is the case plotted in the right panel of Fig. 2.

In Fig. 9, we present the detection rate as a function of the MBH mass ratio  $q = M_2/M_1$ . In the upper panel, besides all the detected sources in **Ecc** run (blue solid curve), **Circ** run (yellow solid curve), and the inspiral sources in the **Ecc** run (blue dashed curve), we also plot the total merger rate in ASTRID (black dotted curve). Most of the LISA sources have a low mass ratio:  $q < 0.1$ . This is because there are more low- $q$  mergers in ASTRID but not because LISA is more sensitive to them. Actually, LISA can observe almost all the mergers with  $q \geq 0.1$ , which is shown by the overlap between the yellow curve and black curve, while a large fraction of low- $q$  mergers is not detectable. Note that the mass ratio has a dependence on the merger mass  $M_{\text{BH}}$ : low- $q$  mergers are dominated by massive mergers, since the secondary MBH mass  $M_2$  is still massive than the adopted black hole seed mass  $10^{4.5} M_\odot$ . This dependence explains why the detection rate for the **Circ** run drops at low- $q$  end, and the enhancement of the detection rate in **Ecc** run at  $q < 0.1$  is consistent with the right panel of Fig. 8.

#### 4. HOST GALAXY AND ENVIRONMENT

An important advantage of using MBH populations from cosmological simulations like ASTRID over those generated by the semi-analytical models (SAMs) is that we can self-consistently associate the MBH merger with their host galaxy. In this section, we focus on the merging populations at two redshifts,  $z = 1.5$  and  $z = 0.8$  to investigate the correlation between the mergers and their local environments. We use the SNR calculated in the **Circ** run to determine the detectable merger population in this section.

##### 4.1. Host galaxies of detected sources

Identifying host galaxies or AGN activities of gravitational wave sources is key to the multi-messenger study of MBHs and has the potential for constraining cosmology. Future detectors like LISA will be able to localize the GW sources to the square-degree level, much better than the current ground-based detectors. However, there are still up to a few hundred candidate galaxies in the LISA source field (Lops et al. 2023). Being able to distinguish the merger hosts from single-MBH galaxies greatly facilitates the EM-followup of LISA events. Recently, Bardati et al. (2024a) and Bardati et al. (2024b) investigated the morphological signatures of MBH merger hosts using cosmological simulation Romulus and found persistent morphological changes in high-mass major mergers. Izquierdo-Villalba et al. (2023) investigated the signatures of LISA source hosts using SAM and found it difficult to identify the

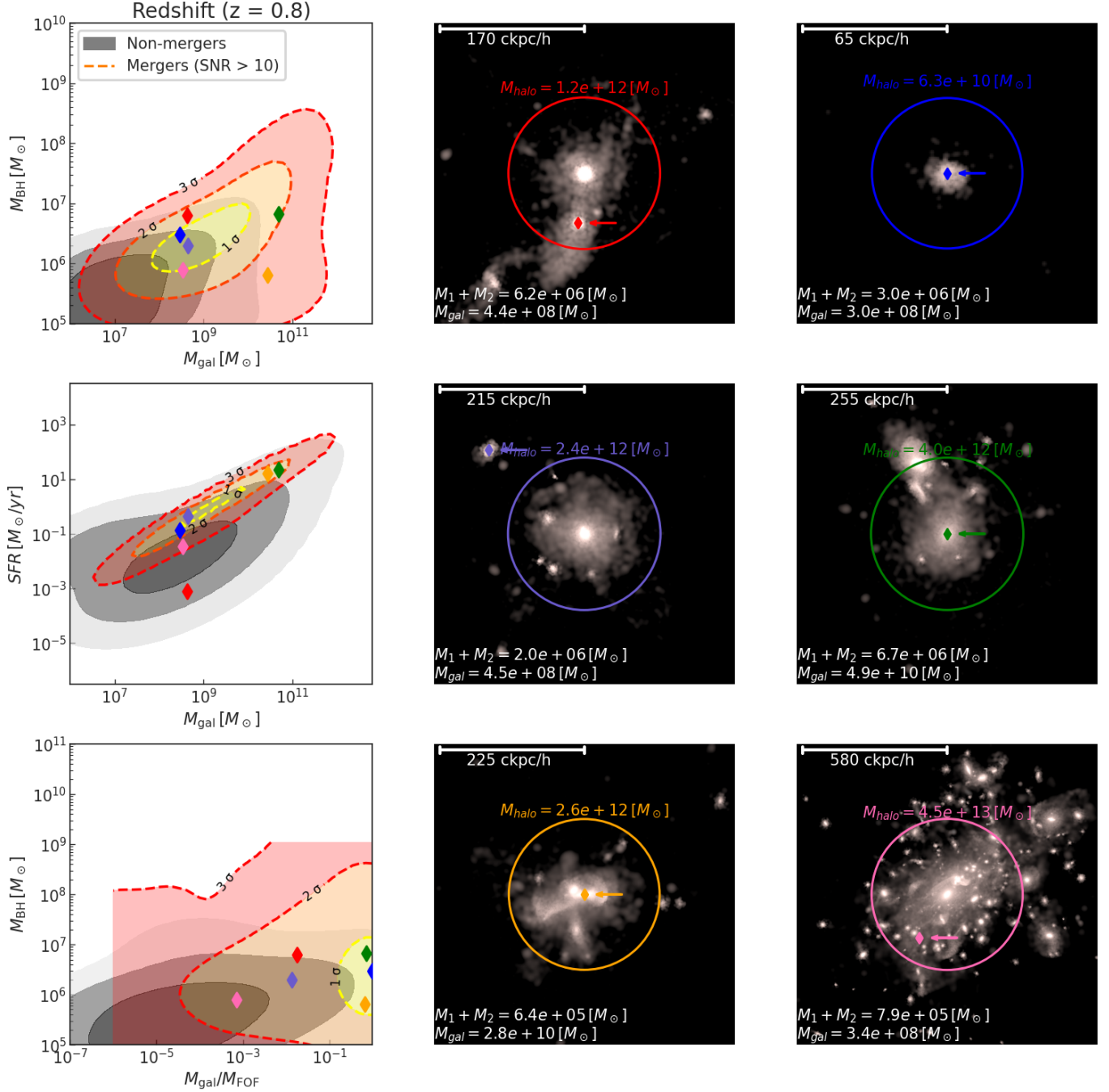


**Figure 10.** The galaxies hosting detectable sources at  $z = 0.8$ . The contour plots in the leftmost column compare the properties of host galaxies of detectable LISA sources which merger within  $0.8 < z < 0.9$  (red contours) and the galaxies hosting no mergers (grey contours). Each contour set plots the  $1\sigma/2\sigma/3\sigma$  regions. *Left Top:* Merger remnant MBH mass versus galaxy stellar mass. *Left Middle:* Star formation rate versus galaxy stellar mass. Note that we remove the galaxies with zero star formation rate to plot this distribution. *Left Bottom:* Merger remnant MBH mass versus the stellar mass ratio between the host galaxy and the FoF halo ( $M_{\text{gal}}/M_{\text{FOF}}$ ). In the top and bottom panels, the non-merging galaxy population uses the central MBH mass for the y-axis as a comparison. We randomly select a sample consisting of 6 detectable sources, which are marked by the diamonds in the contours plots. In the middle and right columns, we plot the stellar density field for the FoF halo for the selected mergers, the location of the remnant MBH is marked by the arrows with corresponding colors. In each frame, the circle represents the virial radius of the halo.



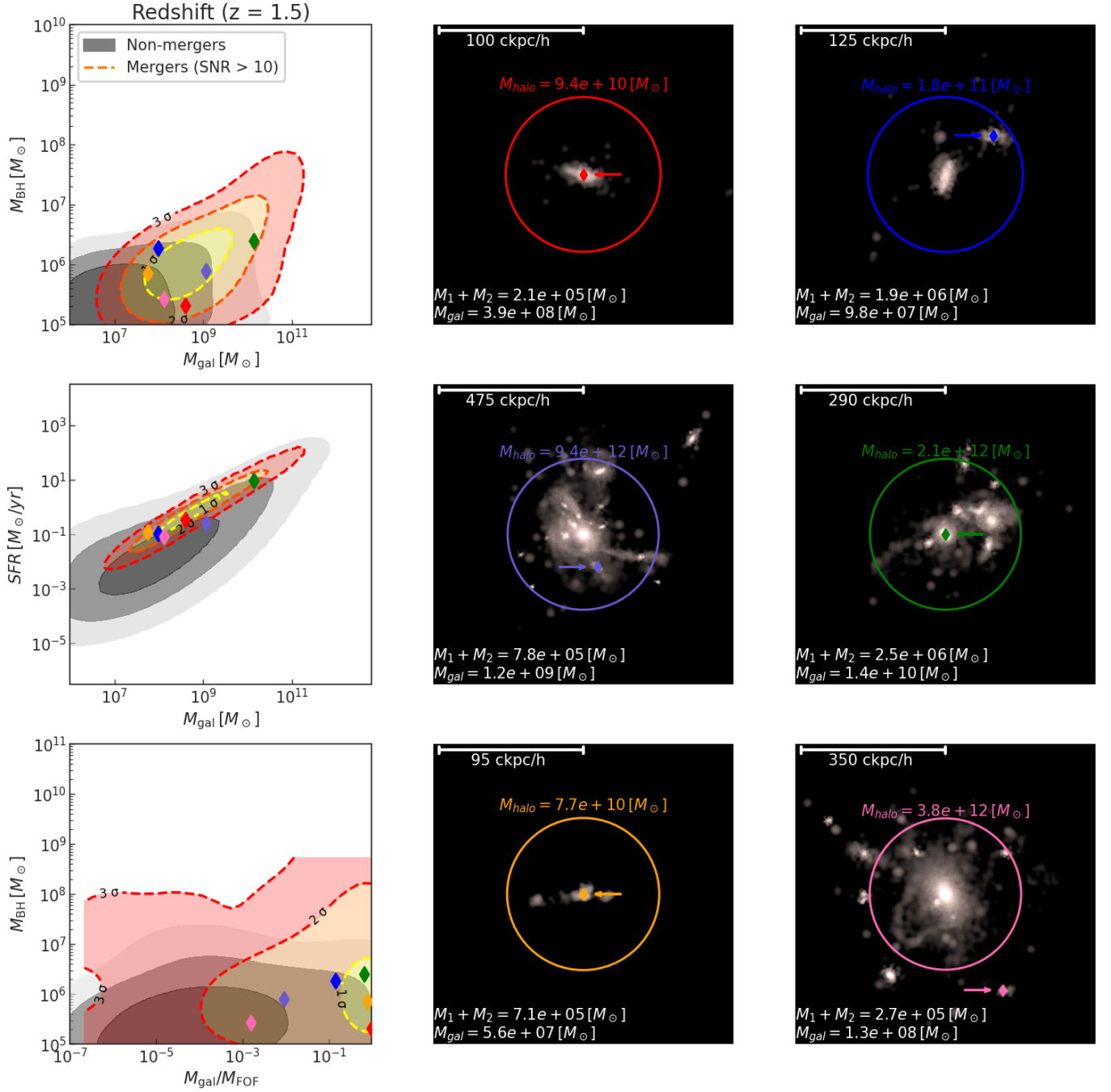


**Figure 11.** Same with Fig. 10, but for the host galaxies of detectable mergers occur within  $1.5 < z < 1.6$ .

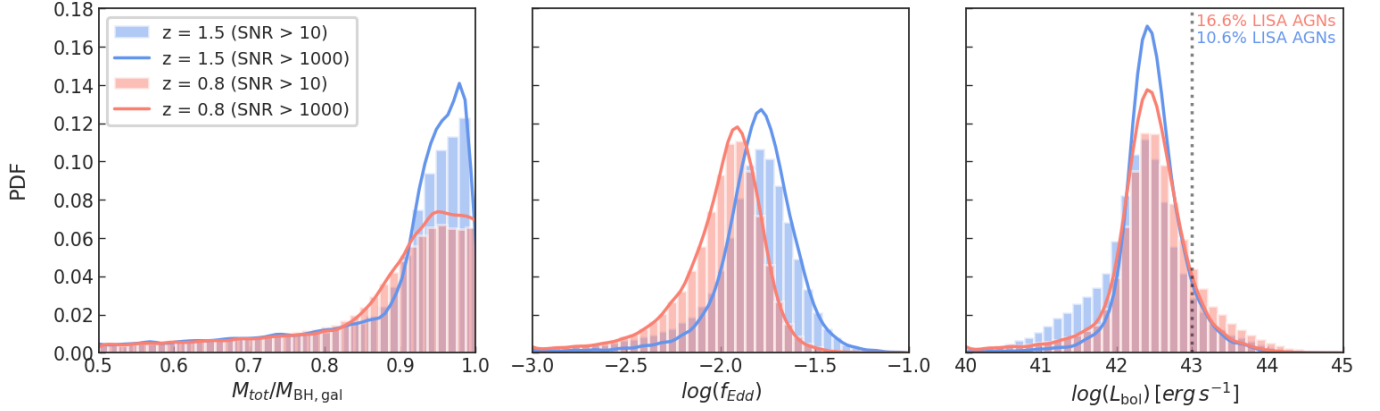


**Figure 12.** 1-D histograms presenting different properties of merging black holes and their subhalo environments. Blue and red correspond to redshifts  $z = 1.5$  and  $z = 0.8$ , respectively. The smooth traces correspond to the distributions of merger events with  $\text{SNR} > 1000$ . *Left:* Ratio of total merger mass ( $M_1 + M_2$ ) to black hole mass in the corresponding subhalo. *Middle:* Black hole Eddington ratio. *Right:* Black hole Bolometric luminosity.

merger hosts solely from the galaxy properties. In this section, we look for distinctive features of MBH merger hosts from the wide range of galaxy population from ASTRID.

In Fig. 10 and 11 we present the properties of the galaxies hosting LISA sources, and compare them to the whole galaxy population in ASTRID at  $z = 0.8$  and  $z = 1.5$ , respectively. In the left column of both figures, the red contours represent the galaxy hosting the MBH mergers detectable by the LISA, i.e.,  $\text{SNR} > 10$ , whose boundaries are highlighted by the dashed lines; and the contours with a grey color scheme correspond to the galaxy population not hosting mergers at that redshift. For each contour set, we plot the  $1\sigma/2\sigma/3\sigma$  regions. From top to bottom, we show the two-dimensional distribution of the MBH mass versus galaxy stellar mass ( $M_{\text{BH}} - M_{\text{gal}}$ , top), galaxy star-formation rate versus galaxy stellar mass ( $\text{SFR} - M_{\text{gal}}$ , middle), and MBH mass versus the stellar mass ratio between the host galaxy and host Friends-of-Friends (FoF) halo ( $M_{\text{BH}} - M_{\text{gal}}/M_{\text{FoF}}$ , bottom). For the galaxies hosting detectable sources, we plot the mass of the remnant MBH as  $M_{\text{BH}}$ ; and for the non-merger galaxies, we plot the mass of the central MBH. At both redshifts, we randomly select a sample consisting of six detectable sources, whose positions among the two-dimensional contours are marked by diamonds. In the middle and right columns, we plot the stellar density field for the FoF halo for the selected mergers. The location of the remnant MBH is marked by symbols with colors corresponding to those used for the same object in the left panels. In each frame, the circle represents the virial radius of the halo.

At both  $z = 0.8$  and  $z = 1.5$ , the galaxies hosting detectable merging sources lie on the same  $M_{\text{BH}} - M_{\text{gal}}$  cor-

relation as the non-merger galaxies, but with differences in how they populate this and the rest of the parameter space. Compared to the non-merger galaxy population, merger hosts have larger galaxy mass on average, with the center of the distribution lying at  $10^9 M_{\odot}$  at both redshifts plotted. This is two orders of magnitude beyond the mean of the non-merger distribution (the latter does depend on the lower mass limit for inclusion into the sample). A significant fraction of the merger hosts are also very massive galaxies with large BHs, with the contour enclosing 95% of the population extending to  $M_{\text{gal}} \sim 10^{11} M_{\odot}$  and  $M_{\text{BH}} \sim 2 - 6 \times 10^{11} M_{\odot}$ . The contours also extend to lower masses, showing that a wide variety of galaxies can be hosts. For example many detectable mergers (of small MBHs) take place in galaxies with masses as small as  $10^7 M_{\odot}$  and below.

The MBH merger hosts are also more star-forming on average, even for a given galaxy mass. At both  $z = 0.8$  and  $z = 1.5$ , an average merger host with galaxy mass between  $10^7 M_{\odot}$  and  $10^{11} M_{\odot}$  has a SFR 50 times higher than the average non-host galaxy of the same mass. The relationship between SFR and galaxy mass is also strikingly tight for mergers compared to the rest of the population, showing that LISA will detect a specific population of objects in this parameter space. We have carried out a power law fit to this sequence of galaxies, of the form:

$$\log(\text{SFR}) = \alpha \log(M_{\text{gal}}) + \beta. \quad (10)$$

For  $z = 0.8$  we find that the slope  $\alpha = 0.88 \pm 0.10$  and the intercept  $\beta = -8.07 \pm 0.90$ . The scatter about this relationship is indeed quite small,  $\sigma_{\text{rms}} \approx 0.17$  dex. The fit values for  $z = 1.5$  are almost the same, and consistent within the errors:  $\alpha = 0.90 \pm 0.09$ ,  $\beta = -8.04 \pm 0.83$ , and  $\sigma_{\text{rms}} \approx 0.14$  dex.

Some merger hosts have SFR of 10-100  $M_{\odot}/\text{yr}$ , and if we examine two of these (the orange and green symbols in Fig. 10 we can see that while both lie at the centers of massive galaxies, one (orange) is in an obviously disturbed ongoing galaxy merger, whereas the green symbol is in a much more uniform and symmetric galaxy. Our merger galaxy masses are similar to those predicted by recent work using SAMs (e.g. Izquierdo-Villalba et al. 2023), but we found a higher contrast in the SFR between merging and single MBH hosts in our simulation.

Looking at the bottom left panels of Figure 10 and 11 that merger hosts are more likely to be the most massive galaxy in a halo. For example, 68% of all merger hosts have a mass greater than  $\sim 20\%$  of that of the FOF halo they reside in, but 68% of non-mergers lie in satellite galaxies with mass less than 0.5% of their FOF halo. Having said this, however, a significant fraction of the merger hosts ( $\sim 20\text{-}30\%$ ) do lie in satellite galaxies in the outskirts of massive halos. For example, among the six examples we have selected and plotted, only half of them are located in the centers of their parent halos, and one of them at each redshift is even hosted by galaxies outside the virial radius (the indigo diamond in Figure 10 and pink diamond in Figure 11). The high probability of merger hosts in isolated halos compared with single MBH hosts may facilitate the EM identification of the LISA sources among the  $> 100$  candidate galaxies in the LISA source field (e.g. Lops et al. 2023).

Our results reveal that LISA will observe MBH mergers in various galaxy environments, covering a wide parameter space of stellar mass and SFR, and in central or satellite galaxies. This is significantly different from the target sources for PTAs. As found in Zhou et al. (2025a), the gravitational continuous (CW) wave sources that have high detection probability for PTAs are all observed in the central galaxies located at the center of galaxy clusters. All of these PTA CW host galaxies have stellar mass over  $10^{12} M_{\odot}$ , and  $\text{SFR} \gtrsim 200 M_{\odot}/\text{yr}$ . Hence, LISA detections will provide complementary information to the MBH mergers that occur in lower-mass galaxies.

#### 4.2. MBH population detected by LISA

In this section, we investigate the MBH population involved in the mergers detected by LISA. In Fig. 12, we show the PDF for the ratio of the merging MBH mass  $M_{\text{tot}} = M_1 + M_2$  to the total MBH mass in the host galaxy (left), the Eddington ratio  $f_{\text{Edd}}$  (middle), and the bolometric luminosity  $L_{\text{bol}}$  (right). In each panel, we plot the detectable sources with SNR larger than 10

(histograms) and with  $\text{SNR} > 1000$  (curves) for  $z = 1.5$  (blue) and  $z = 0.8$ , respectively.

From the distribution of  $M_{\text{tot}}/M_{\text{BH,gal}}$ , we can see that in roughly half of host galaxies, merging binaries constitute over 90% of the total black hole mass. This means that the remnant MBHs are typically the galaxy central black hole. The distribution is similar at  $z = 0.8$  and  $z = 1.5$ , except that at  $z = 1.5$ , there are more sources with masses over 90% of the total BH mass, while there are more remnant MBHs which have mass between  $0.8 \sim 0.9 M_{\text{BH,gal}}$  at  $z = 0.8$ . This can be explained by the larger galaxies at lower redshift, which host many more small-mass wandering MBHs.

We then investigate the accretion efficiency of the merging MBHs. The peak of the Eddington ratio  $f_{\text{Edd}} = L_{\text{bol}}/L_{\text{edd}}$  the  $f_{\text{edd}}$  distribution is skewed to lower values at lower redshift: at  $z = 1.5$  the peak is  $\log(f_{\text{edd}}) = -1.75$  which evolves to  $\log(f_{\text{edd}}) = -2$  by  $z = 0.8$ .

Unlike the Eddington ratio,  $L_{\text{bol}}$  peaks around  $\log(L_{\text{bol}}) \sim 42.5 \text{ erg/s}$  for both  $z = 0.8$  and  $z = 1.5$ , while the high- $z$  distribution has a larger low-luminosity tail. Defining the MBHs with  $L_{\text{bol}} > 10^{43} \text{ erg/s}$  as AGN (Chen et al. 2023) (marked by the vertical black dotted line in the right panel in Fig. 12) we find that only 10.6% of detectable (i.e., with SNR larger than 10) sources involve AGN activity at  $z = 1.5$ , and 16.6% at  $z = 0.8$ . Thus only a small fraction of LISA sources will have detectable electromagnetic counterparts. We check that most of these mergers involving the AGNs are from massive mergers with  $M_{\text{tot}} \gtrsim 10^{6.5} M_{\odot}$ . Recently, Dong-Páez et al. (2023) also investigated the AGN signatures of LISA sources, but at a higher redshift of  $z \sim 3.5$ , and found 4  $\sim 20\%$  of sources to be detectable through AGN signatures. Our results are in general agreements despite the different source redshift distributions.

## 5. DISCUSSION

### 5.1. The Influence of Eccentricity

As we show in Fig. 7 and 8, including the effect of eccentricity (the Ecc run) enhances the detectability of events with LISA. The detectable mass range expands from  $10^8 M_{\odot}$  to  $10^9 M_{\odot}$ , and the detection rate at low redshift ( $z < 0.5$ ) and at high mass ( $M_{\text{BH}} > 10^{7.5} M_{\odot}$ ) increases by an order of magnitude. In this section we discuss in detail how the eccentricity makes such a difference.

In the period a few years before coalescence, the eccentricity of a binary will rapidly reduce via GW emission driven circularization. If this circularization process causes the eccentricity to reach close to zero, or the dominant harmonic mode becomes close to  $n = 2$ , we find

that the behavior of the **Ecc** run is very similar to that of the **Circ** run (shown in the left and middle panels of Fig. 2). Since the total SNR is typically dominated by the emission in the short phase before coalescence, these fully circularized sources have similar detectability in both the **Ecc** and **Circ** runs. The difference in the detectable population for **Ecc** and **Circ** runs thus mainly comes from mergers with large residual eccentricity.

One caveat about the **Ecc** run is that we directly adopt the orbital eccentricity measured from ASTRID as the value at  $t_{\text{start}}$ , i.e., the initial eccentricity observed by LISA. The hardening timescale for binaries to evolve from  $\sim 1$  kpc into the GW-emitting regime could be over 1 Gyr (Chen et al. 2020; Kelley et al. 2017), and the eccentricity evolution during this process is dependent on the local galaxy environment. As shown by Sesana (2010), stellar dynamics causes a dramatic increase in orbital eccentricity, especially for initially already mildly eccentric and/or unequal mass binaries. In the MAGICs simulation suite (Chen et al. 2024; Zhou et al. 2025b; Mukherjee et al. 2025), the authors found that the orbital eccentricities increase during the evolution of the bound binary, but are constant once hard binaries form. Romero-Shaw et al. (2024) showed that binaries driven by the circumbinary disc will evolve to an equilibrium eccentricity:  $0.2 \lesssim e_{\text{eq}} \lesssim 0.5$ . More importantly, when the binary is observed at  $t_{\text{start}}$ , it is likely that it has gone through GW circularization since the GW emission timescale is typically over 100 years. For the observed merger sources for which  $t_{\text{obs}}$  is within 4 years of the merger and which have rapidly decreasing eccentricity, circularization becomes the dominant effect. Considering that most of our detected sources are merger sources (see Fig. 8), the LISA sources in our current work are therefore those with higher eccentricities. In future work, we plan to implement an eccentricity evolution model, which depends on the local environment of each binary, such as the stellar profile index and density, to track the eccentricity evolution of the unbound binaries in a more self-consistent way.

### 5.2. Binary Delayed Timescale

In this work, we do not apply any binary delay model to account for the evolution timescale from a 1 kpc separation (i.e., the resolution limit of ASTRID) to the GW regime. Considering unresolved dynamical friction and stellar scattering, Chen et al. (2022b) estimated the hardening timescale for the MBH binary population in ASTRID with  $z > 3$ . Incorporating the delay time, it was found that the decrease in the resultant detection rate is smaller than one order of magnitude. Katz et al. (2020) evolved the MBH merger population in Illustris

by post-processing using the treatments of Kelley et al. (2017) and Dosopoulou & Antonini (2017), and found that the detection rate only drops by a maximum of half. Salcido et al. (2016) came to a similar conclusion: the merger rate is similar across all hardening models, and their impact is much smaller than the impact of changing the black hole seed mass adopted. These previous analyses imply that including the binary delay may only change in a minor fashion for the predicted detection rate plotted in Fig. 8.

## 6. CONCLUSION

In this work, we estimate the GW signal emitted by MBH mergers down to  $z = 0$  in the cosmological simulation ASTRID, and make predictions for the LISA detection rate.

Using the recorded trajectories of MBHs in ASTRID, we are able to measure the orbital eccentricity  $e$  of merging objects. We find that the MBH mergers in general have high eccentricity:  $e$  peaks at  $\gtrsim 0.8$  across the whole redshift range. It evolves slightly to smaller values at low redshift: from 0.88 at  $z > 3$  to 0.80 at  $z < 0.5$ , indicating that a larger fraction of binaries at low redshift merge with circular orbits. This can be explained by the shorter hardening timescales for binaries with high eccentricity (Chen et al. 2022b). To give a better description of the  $e$  distribution, we provide a fitted  $e$  PDF function (Equation 9), which includes the redshift evolution.

To investigate the influence of eccentricity on GW emission in the LISA band ( $10^{-5} < f < 1$  Hz) we generate two sets of signals: a **Circ** run that assumes circular orbits for all the sources, and a **Ecc** run that includes the effect of eccentricity in the calculation of GW waveforms. Given the black hole seed masses in ASTRID of  $M_{\text{BH,seed}} \sim 5 \times 10^4 M_{\odot}$ , we find that LISA will probe MBH mergers across a wide parameter space, covering objects with  $M_{\text{BH}} \lesssim 10^9 M_{\odot}$  and  $z \lesssim 8$ .

We implement a Monte Carlo analysis technique to estimate the LISA detection rate. This enables us to generate multiple realizations of the merger population detectable by LISA, and avoids the assumption of a specific observation time for each MBH binary. We can therefore consider the signals emitted from different binary evolution phases, i.e., from both inspiral sources and merging sources. We generate 10,000 realizations of the merging MBH populations that would be detected by a 4-year LISA observation. Our prediction is averaged over these realizations: The total LISA detection rate predicted by ASTRID is 5.6/yr for the **Circ** run and 10.5/yr for the **Ecc** run. Among them, 46% (4.8



events per year) are inspiral sources for **Ecc**, and only 0.3% ( $\sim 10^{-4}$  event per year) are for **Circ**.

While the detectable parameter space for the eccentric and circular binaries largely overlaps, including the eccentricity will expand the detectable mass range by one order of magnitude: from  $M_{\text{BH}} \sim 10^8 M_{\odot}$  to  $\sim 10^9 M_{\odot}$ . The redshift peak for the LISA sources also shifts to a lower value in the **Ecc** run ( $z_{\text{peak}} = 0.8$  compared to the **Circ** run ( $z_{\text{peak}}$  of  $z = 1.9$ ). At low redshift ( $z < 0.5$ ) and high BH mass ( $M_{\text{bh}} > 10^{7.5} M_{\odot}$ ), the **Ecc** run predicts a detection rate one order of magnitude higher than **Circ** run. The improvement in detectability comes from the inspiral sources, which coalesce after the 4-year LISA observation phase. The residual eccentricity in the inspiral phase produces waveforms covering a wide frequency range and GW signals better matched to the LISA high-sensitivity band. Our results underscore the importance of incorporating the orbital eccentricity in the predictions for upcoming GW detection, which requires accurately modeling the dynamics of MBH binaries and their merger histories.

We also investigate the host galaxies of detectable mergers. Unlike the PTA CW sources, the LISA detectable mergers will be observed to lie in various galaxy environments, covering a wide range of mass ( $10^7 - 10^{11} M_{\odot}$ ), and SFR ( $10^{-3} - 10^2 M_{\odot}/\text{yr}$ ). Notably, a significant fraction ( $\sim 20 - 30\%$ ) of the detectable sources

occur in satellite galaxies, sometimes even outside the virial radius. The merger hosts are also much more highly star forming than the general population, with a mean SFR fifty times higher for a given galaxy mass. The relationship between SFR and galaxy mass for merging MBHs is tight, tracing a distinct population, and this sequence is well described by a power law where  $\text{SFR} = 10^{-8} M_{\text{gal}}^{0.9} M_{\odot}/\text{yr}$ , with a scatter of 0.17 dex. Most of the remnant MBHs are the central MBH of the galaxy, while only a small fraction (about 10%) are AGNs with a bolometric luminosity larger than  $10^{43}$  erg/s. This implies that it will be difficult to search for the electromagnetic counterpart of LISA sources.

## ACKNOWLEDGEMENTS

BYW thanks Yili Han and Handan Zhang for their helpful advice on the visualization. TDM acknowledges funding from NASA ATP 80NSSC20K0519, NSF PHY-2020295, NASA ATP NNX17AK56G, and NASA ATP 80NSSC18K101, NASA Theory grant 80NSSC22K072. NC acknowledges support from the Schmidt Futures Fund. YN acknowledges support from the ITC Postdoctoral Fellowship. SB acknowledges funding from NASA ATP 80NSSC22K1897. ASTRID was run on the Frontera facility at the Texas Advanced Computing Center.

## REFERENCES

- Abbott, B. P., Abbott, R., Abbott, T. D., et al. 2016, *PhRvL*, 116, 061102, doi: [10.1103/PhysRevLett.116.061102](https://doi.org/10.1103/PhysRevLett.116.061102)
- Agazie, G., Anumalapudi, A., Archibald, A. M., et al. 2023, *ApJL*, 951, L8, doi: [10.3847/2041-8213/acdac6](https://doi.org/10.3847/2041-8213/acdac6)
- Amaro-Seoane, P., Sesana, A., Hoffman, L., et al. 2010, *MNRAS*, 402, 2308, doi: [10.1111/j.1365-2966.2009.16104.x](https://doi.org/10.1111/j.1365-2966.2009.16104.x)
- Amaro-Seoane, P., Audley, H., Babak, S., et al. 2017a, arXiv e-prints, arXiv:1702.00786, doi: [10.48550/arXiv.1702.00786](https://doi.org/10.48550/arXiv.1702.00786)
- . 2017b, arXiv e-prints, arXiv:1702.00786, doi: [10.48550/arXiv.1702.00786](https://doi.org/10.48550/arXiv.1702.00786)
- Arun, K. G., Babak, S., Berti, E., et al. 2009, *Classical and Quantum Gravity*, 26, 094027, doi: [10.1088/0264-9381/26/9/094027](https://doi.org/10.1088/0264-9381/26/9/094027)
- Arzoumanian, Z., Brazier, A., Burke-Spolaor, S., et al. 2018, *ApJS*, 235, 37, doi: [10.3847/1538-4365/aab5b0](https://doi.org/10.3847/1538-4365/aab5b0)
- Barausse, E. 2012, *MNRAS*, 423, 2533, doi: [10.1111/j.1365-2966.2012.21057.x](https://doi.org/10.1111/j.1365-2966.2012.21057.x)
- Bardati, J., Ruan, J. J., Haggard, D., & Tremmel, M. 2024a, *ApJ*, 961, 34, doi: [10.3847/1538-4357/ad055a](https://doi.org/10.3847/1538-4357/ad055a)
- Bardati, J., Ruan, J. J., Haggard, D., Tremmel, M., & Horlaville, P. 2024b, *ApJ*, 977, 265, doi: [10.3847/1538-4357/ad9471](https://doi.org/10.3847/1538-4357/ad9471)
- Bird, S., Ni, Y., Di Matteo, T., et al. 2022, *MNRAS*, 512, 3703, doi: [10.1093/mnras/stac648](https://doi.org/10.1093/mnras/stac648)
- Bondi, H., & Hoyle, F. 1944, *MNRAS*, 104, 273
- Chattaraj, A., RoyChowdhury, T., Divyajyoti, Chandra Kant, M., & Gupta, A. 2022, *PhRvD*, 106, 124008, doi: [10.1103/PhysRevD.106.124008](https://doi.org/10.1103/PhysRevD.106.124008)
- Chen, N., Mukherjee, D., Di Matteo, T., et al. 2024, *The Open Journal of Astrophysics*, 7, 28, doi: [10.33232/001c.116179](https://doi.org/10.33232/001c.116179)
- Chen, N., Ni, Y., Tremmel, M., et al. 2022a, *MNRAS*, 510, 531, doi: [10.1093/mnras/stab3411](https://doi.org/10.1093/mnras/stab3411)
- Chen, N., Ni, Y., Holgado, A. M., et al. 2022b, *MNRAS*, 514, 2220, doi: [10.1093/mnras/stac1432](https://doi.org/10.1093/mnras/stac1432)
- Chen, N., Di Matteo, T., Ni, Y., et al. 2023, *MNRAS*, 522, 1895, doi: [10.1093/mnras/stad834](https://doi.org/10.1093/mnras/stad834)

- Chen, Y., Yu, Q., & Lu, Y. 2020, *ApJ*, 897, 86, doi: [10.3847/1538-4357/ab9594](https://doi.org/10.3847/1538-4357/ab9594)
- Crain, R. A., Schaye, J., Bower, R. G., et al. 2015, *MNRAS*, 450, 1937, doi: [10.1093/mnras/stv725](https://doi.org/10.1093/mnras/stv725)
- DeGraf, C., Chen, N., Ni, Y., et al. 2024, *MNRAS*, 527, 11766, doi: [10.1093/mnras/stad3084](https://doi.org/10.1093/mnras/stad3084)
- Desvignes, G., Caballero, R. N., Lentati, L., et al. 2016, *MNRAS*, 458, 3341, doi: [10.1093/mnras/stw483](https://doi.org/10.1093/mnras/stw483)
- Dong-Páez, C. A., Volonteri, M., Beckmann, R. S., et al. 2023, *A&A*, 676, A2, doi: [10.1051/0004-6361/202346435](https://doi.org/10.1051/0004-6361/202346435)
- Dosopoulou, F., & Antonini, F. 2017, *ApJ*, 840, 31, doi: [10.3847/1538-4357/aa6b58](https://doi.org/10.3847/1538-4357/aa6b58)
- EPTA Collaboration, InPTA Collaboration, Antoniadis, J., et al. 2023, *A&A*, 678, A50, doi: [10.1051/0004-6361/202346844](https://doi.org/10.1051/0004-6361/202346844)
- Feng, Y., Bird, S., Anderson, L., Font-Ribera, A., & Pedersen, C. 2018, MP-Gadget/MP-Gadget: A tag for getting a DOI, FirstDOI, Zenodo, doi: [10.5281/zenodo.1451799](https://doi.org/10.5281/zenodo.1451799)
- Ferrarese, L. 2002, *ApJ*, 578, 90, doi: [10.1086/342308](https://doi.org/10.1086/342308)
- Ferrarese, L., & Merritt, D. 2000, *ApJL*, 539, L9, doi: [10.1086/312838](https://doi.org/10.1086/312838)
- Finn, L. S., & Thorne, K. S. 2000, *PhRvD*, 62, 124021, doi: [10.1103/PhysRevD.62.124021](https://doi.org/10.1103/PhysRevD.62.124021)
- Graham, A. W., Erwin, P., Caon, N., & Trujillo, I. 2001, *ApJL*, 563, L11, doi: [10.1086/338500](https://doi.org/10.1086/338500)
- Greene, J. E., Seth, A., Kim, M., et al. 2016, VizieR Online Data Catalog: Black hole masses in megamaser disk galaxies (Greene+, 2016), VizieR On-line Data Catalog: J/ApJ/826/L32. Originally published in: 2016ApJ...826L..32G, doi: [10.26093/cds/vizier.18269032](https://doi.org/10.26093/cds/vizier.18269032)
- Gültekin, K., Richstone, D. O., Gebhardt, K., et al. 2009, *ApJ*, 698, 198, doi: [10.1088/0004-637X/698/1/198](https://doi.org/10.1088/0004-637X/698/1/198)
- Hinder, I., Kidder, L. E., & Pfeiffer, H. P. 2018, *Phys. Rev. D*, 98, 044015, doi: [10.1103/PhysRevD.98.044015](https://doi.org/10.1103/PhysRevD.98.044015)
- Hiscock, W. A., Larson, S. L., Routzahn, J. R., & Kulick, B. 2000, *ApJL*, 540, L5, doi: [10.1086/312867](https://doi.org/10.1086/312867)
- Husa, S., Khan, S., Hannam, M., et al. 2016, *PhRvD*, 93, 044006, doi: [10.1103/PhysRevD.93.044006](https://doi.org/10.1103/PhysRevD.93.044006)
- Izquierdo-Villalba, D., Colpi, M., Volonteri, M., et al. 2023, *A&A*, 677, A123, doi: [10.1051/0004-6361/202347008](https://doi.org/10.1051/0004-6361/202347008)
- Izquierdo-Villalba, D., Sesana, A., Colpi, M., et al. 2024, *A&A*, 686, A183, doi: [10.1051/0004-6361/202449293](https://doi.org/10.1051/0004-6361/202449293)
- Katz, M. L., Kelley, L. Z., Dosopoulou, F., et al. 2020, *MNRAS*, 491, 2301, doi: [10.1093/mnras/stz3102](https://doi.org/10.1093/mnras/stz3102)
- Katz, M. L., & Larson, S. L. 2019, *MNRAS*, 483, 3108, doi: [10.1093/mnras/sty3321](https://doi.org/10.1093/mnras/sty3321)
- Kelley, L. Z., Blecha, L., & Hernquist, L. 2017, *MNRAS*, 464, 3131, doi: [10.1093/mnras/stw2452](https://doi.org/10.1093/mnras/stw2452)
- Khan, S., Husa, S., Hannam, M., et al. 2016, *PhRvD*, 93, 044007, doi: [10.1103/PhysRevD.93.044007](https://doi.org/10.1103/PhysRevD.93.044007)
- Klein, A., Barausse, E., Sesana, A., et al. 2016, *PhRvD*, 93, 024003, doi: [10.1103/PhysRevD.93.024003](https://doi.org/10.1103/PhysRevD.93.024003)
- Kormendy, J., & Ho, L. C. 2013, *ARA&A*, 51, 511, doi: [10.1146/annurev-astro-082708-101811](https://doi.org/10.1146/annurev-astro-082708-101811)
- Kormendy, J., & Richstone, D. 1995, *ARA&A*, 33, 581, doi: [10.1146/annurev.aa.33.090195.003053](https://doi.org/10.1146/annurev.aa.33.090195.003053)
- Li, K., Bogdanović, T., Ballantyne, D. R., & Bonetti, M. 2022, *ApJ*, 933, 104, doi: [10.3847/1538-4357/ac74b5](https://doi.org/10.3847/1538-4357/ac74b5)
- . 2023, *ApJ*, 959, 3, doi: [10.3847/1538-4357/ad04d2](https://doi.org/10.3847/1538-4357/ad04d2)
- Lops, G., Izquierdo-Villalba, D., Colpi, M., et al. 2023, *MNRAS*, 519, 5962, doi: [10.1093/mnras/stad058](https://doi.org/10.1093/mnras/stad058)
- Magorrian, J., Tremaine, S., Richstone, D., et al. 1998, *AJ*, 115, 2285, doi: [10.1086/300353](https://doi.org/10.1086/300353)
- McConnell, N. J., & Ma, C.-P. 2013, *ApJ*, 764, 184, doi: [10.1088/0004-637X/764/2/184](https://doi.org/10.1088/0004-637X/764/2/184)
- Merritt, D. 2013, Dynamics and Evolution of Galactic Nuclei
- Miller, J. M. 2007, *ARA&A*, 45, 441, doi: [10.1146/annurev.astro.45.051806.110555](https://doi.org/10.1146/annurev.astro.45.051806.110555)
- Moore, C. J., Cole, R. H., & Berry, C. P. L. 2015, *Classical and Quantum Gravity*, 32, 015014, doi: [10.1088/0264-9381/32/1/015014](https://doi.org/10.1088/0264-9381/32/1/015014)
- Mukherjee, D., Zhou, Y., Chen, N., Di Carlo, U. N., & Di Matteo, T. 2025, *ApJ*, 981, 203, doi: [10.3847/1538-4357/adb1b0](https://doi.org/10.3847/1538-4357/adb1b0)
- Ni, Y., Chen, N., Zhou, Y., et al. 2024, arXiv e-prints, arXiv:2409.10666, doi: [10.48550/arXiv.2409.10666](https://doi.org/10.48550/arXiv.2409.10666)
- Ni, Y., Di Matteo, T., Bird, S., et al. 2022, *MNRAS*, 513, 670, doi: [10.1093/mnras/stac351](https://doi.org/10.1093/mnras/stac351)
- Peters, P. C., & Mathews, J. 1963, *Physical Review*, 131, 435, doi: [10.1103/PhysRev.131.435](https://doi.org/10.1103/PhysRev.131.435)
- Planck Collaboration, Aghanim, N., Akrami, Y., et al. 2020, *A&A*, 641, A6, doi: [10.1051/0004-6361/201833910](https://doi.org/10.1051/0004-6361/201833910)
- Reardon, D. J., Hobbs, G., Coles, W., et al. 2016, *MNRAS*, 455, 1751, doi: [10.1093/mnras/stv2395](https://doi.org/10.1093/mnras/stv2395)
- Reardon, D. J., Zic, A., Shannon, R. M., et al. 2023, *ApJL*, 951, L6, doi: [10.3847/2041-8213/acdd02](https://doi.org/10.3847/2041-8213/acdd02)
- Reines, A. E., & Volonteri, M. 2015, *ApJ*, 813, 82, doi: [10.1088/0004-637X/813/2/82](https://doi.org/10.1088/0004-637X/813/2/82)
- Reynolds, C. S. 2013, *Classical and Quantum Gravity*, 30, 244004, doi: [10.1088/0264-9381/30/24/244004](https://doi.org/10.1088/0264-9381/30/24/244004)
- Rodríguez-Gomez, V., Genel, S., Vogelsberger, M., et al. 2015, *MNRAS*, 449, 49, doi: [10.1093/mnras/stv264](https://doi.org/10.1093/mnras/stv264)
- Romero-Shaw, I. M., Goorachurn, S., Siwek, M., & Moore, C. J. 2024, *MNRAS*, 534, L58, doi: [10.1093/mnrasl/slaf081](https://doi.org/10.1093/mnrasl/slaf081)
- Salcido, J., Bower, R. G., Theuns, T., et al. 2016, *MNRAS*, 463, 870, doi: [10.1093/mnras/stw2048](https://doi.org/10.1093/mnras/stw2048)

- Schaye, J., Crain, R. A., Bower, R. G., et al. 2015, MNRAS, 446, 521, doi: [10.1093/mnras/stu2058](https://doi.org/10.1093/mnras/stu2058)
- Schutte, Z., Reines, A. E., & Greene, J. E. 2019, ApJ, 887, 245, doi: [10.3847/1538-4357/ab35dd](https://doi.org/10.3847/1538-4357/ab35dd)
- Sesana, A. 2010, ApJ, 719, 851, doi: [10.1088/0004-637X/719/1/851](https://doi.org/10.1088/0004-637X/719/1/851)
- Sesana, A., Gair, J., Berti, E., & Volonteri, M. 2011, PhRvD, 83, 044036, doi: [10.1103/PhysRevD.83.044036](https://doi.org/10.1103/PhysRevD.83.044036)
- Sesana, A., Volonteri, M., & Haardt, F. 2007, MNRAS, 377, 1711, doi: [10.1111/j.1365-2966.2007.11734.x](https://doi.org/10.1111/j.1365-2966.2007.11734.x)
- Setyawati, Y., & Ohme, F. 2021, Phys. Rev. D, 103, 124011, doi: [10.1103/PhysRevD.103.124011](https://doi.org/10.1103/PhysRevD.103.124011)
- Shakura, N. I., & Sunyaev, R. A. 1973, A&A, 24, 337
- Tremmel, M., Governato, F., Volonteri, M., & Quinn, T. R. 2015, MNRAS, 451, 1868, doi: [10.1093/mnras/stv1060](https://doi.org/10.1093/mnras/stv1060)
- Tremmel, M., Governato, F., Volonteri, M., Quinn, T. R., & Pontzen, A. 2018, MNRAS, 475, 4967, doi: [10.1093/mnras/sty139](https://doi.org/10.1093/mnras/sty139)
- Vogelsberger, M., Genel, S., Springel, V., et al. 2014, MNRAS, 444, 1518, doi: [10.1093/mnras/stu1536](https://doi.org/10.1093/mnras/stu1536)
- Volonteri, M., Pfister, H., Beckmann, R. S., et al. 2020, MNRAS, 498, 2219, doi: [10.1093/mnras/staa2384](https://doi.org/10.1093/mnras/staa2384)
- Wagg, T., Breivik, K., & de Mink, S. E. 2022, ApJS, 260, 52, doi: [10.3847/1538-4365/ac5c52](https://doi.org/10.3847/1538-4365/ac5c52)
- Weinberger, R., Springel, V., Hernquist, L., et al. 2017, MNRAS, 465, 3291, doi: [10.1093/mnras/stw2944](https://doi.org/10.1093/mnras/stw2944)
- Wyithe, J. S. B., & Loeb, A. 2003, ApJ, 590, 691, doi: [10.1086/375187](https://doi.org/10.1086/375187)
- Xu, H., Chen, S., Guo, Y., et al. 2023, Research in Astronomy and Astrophysics, 23, 075024, doi: [10.1088/1674-4527/acdfa5](https://doi.org/10.1088/1674-4527/acdfa5)
- Zhou, Y., Di Matteo, T., Chen, N., et al. 2025a, arXiv e-prints, arXiv:2502.01845, doi: [10.48550/arXiv.2502.01845](https://doi.org/10.48550/arXiv.2502.01845)
- Zhou, Y., Mukherjee, D., Chen, N., et al. 2025b, ApJ, 980, 79, doi: [10.3847/1538-4357/ada283](https://doi.org/10.3847/1538-4357/ada283)